

RA 623073

RADC-TR-65-186, Vol. II  
Final Report

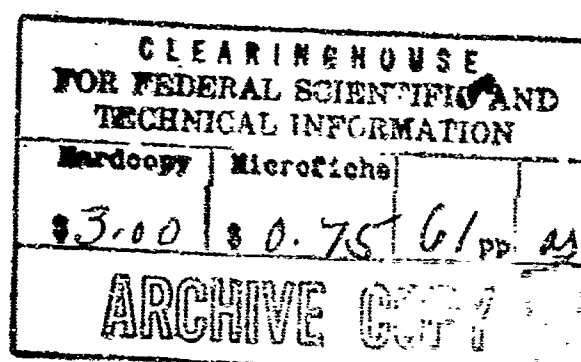


## ANTENNA LOBE SUPPRESSION

Volume II - The E-Plane Radiation Pattern of an Antenna  
Model for Horn Antennas

J. S. Yu  
R. C. Rudduck

TECHNICAL REPORT NO. RADC-TR-65-186  
October 1965



Vulnerability Reduction Branch  
Rome Air Development Center  
Research and Technology Division  
Air Force Systems Command  
Griffiss Air Force Base, New York

When US Government drawings, specifications, or other data are used for any purpose other than a definitely related government procurement operation, the government thereby incurs no responsibility nor any obligation whatsoever; and the fact that the government may have formulated, furnished, or in any way supplied the said drawings, specifications, or other data is not to be regarded by implication or otherwise, as in any manner licensing the holder or any other person or corporation, or conveying any rights or permission to manufacture, use, or sell any patented invention that may in any way be related thereto

Do not return this copy. Retain or destroy.

## ANTENNA LOBE SUPPRESSION

Volume II - The E-Plane Radiation Pattern of an Antenna  
Model for Horn Antennas

J. S. Yu  
R. C. Rudduck

## ABSTRACT

Diffraction theory is used in analyzing the radiation characteristics of typical horn antennas. The far-side-lobe and back-lobe radiation has been solved without employing equivalence principles which are impractical in the problem.

A corner reflector with a magnetic line source located at the vertex is proposed as a model for the E-plane radiation of horn antennas. Diffraction theory is applied to formulate the radiation pattern of this antenna model. A complete pattern, including multiple interactions and images of induced line sources, is obtained in infinite series form. Diffraction mechanisms are used for appropriate approximations in the computations. Emphasis is made on the continuity of the radiation patterns. The computed patterns are in excellent agreement with measured patterns of typical horn antennas. Radiation intensity of the back-lobe relative to main-lobe intensity is obtained as back-to-front ratio and plotted as a function of antenna dimensions. A set of measured back-to-front ratios is presented to demonstrate the validity of computation.

## TABLE OF CONTENTS

	Page
I. INTRODUCTION	1
II. RADIATION MECHANISMS	2
III. FORMULATION OF SOLUTION IN INFINITE SERIES FORM	5
IV. THE APPROXIMATED SOLUTIONS	16
V. COMPUTED PATTERNS COMPARED WITH MEASURED PATTERNS OF HORN ANTENNAS	21
VI. RELATIVE BACK LEVELS	24
VII. CONCLUSIONS	29
ACKNOWLEDGEMENTS	30
APPENDIX A - REVIEW OF DIFFRACTION THEORY	31
APPENDIX B - FAR-FIELD WAVES FROM THE IMAGES OF LINE SOURCES	36
APPENDIX C - COUPLING COEFFICIENTS OF THE FOUR WEDGES OF THE ANTENNA MODEL	42

TABLE OF CONTENTS (cont).

	Page
APPENDIX D - THE SCATRAN SOURCE PROGRAMS FOR NUMERICAL COMPUTATION BY IBM 7094	47
REFERENCES	54

## THE E-PLANE RADIATION PATTERN OF AN ANTENNA MODEL FOR HORN ANTENNAS

### I. INTRODUCTION

Electromagnetic horns are widely used either as feeds or direct radiators in antenna systems. Therefore, a complete and practical understanding of the radiation mechanisms is important. The purpose here is to provide this understanding by using diffraction theory as a tool for analyzing radiation characteristics of horn antennas.

Experimentally radiation patterns of different horn lengths and flare angles in both E- and H-planes have been measured by Rhodes[1]. These patterns are adequate only in the vicinity of the main lobe. For the regions of the far side-lobes and back lobes, which are important in EMC (Electromagnetic Compatibility) problems, more accurate measurements are required.

Analytically, the descriptions of the propagating modes in a horn are summarized by Kraus[2]. In general, aperture techniques must be used to calculate the radiation pattern, and it is assumed that the aperture distribution is that of the incident wave and is zero outside the aperture. The patterns thus obtained give satisfactory main lobes and near side-lobes. As for far side-lobes and back lobes, Schelkonoff's equivalence principles could be applied if current distributions on the outer surfaces were known. For a horn antenna, extreme difficulty is involved in accurately describing the current distributions. Furthermore, difficulty would arise in evaluating the consequent surface integrals. The impracticality of the equivalence principles leaves radiation problems of the far side-lobes and back lobes still unsolved.

Because of the increasing power levels of individual antennas and the increasing numbers of radiating systems in particular areas, the characteristics of far side-lobes and back lobes have become increasingly important in EMC problems. Since these radiation characteristics are caused by diffraction of electromagnetic waves, it has been a natural consequence in recent years to apply diffraction theory to the radiation problems of horn antennas.

In 1962, Kinber [3] derived horn patterns and the coefficient of coupling between two adjacent horns by diffraction theory. Examples are given for both E-plane and H-plane patterns, in which discontinuities are pointed out, and emphasis has not been made on side and back lobes. In 1963 Ohba[4] used diffraction theory to compute the radiation pattern in the H-plane of a corner reflector. Disagreement was noted as a result of neglecting contributions from the other edges of the corner reflector. In 1964, Russo, Rudduck, and Peters[5] employed diffraction theory with proper assumptions to obtain E-plane patterns of a thin-edged and a thick-edged horn. Only the first-order diffraction terms were used to compute the thin-edged horn patterns. The results, with possible discontinuities left in the side and back lobes, are in good agreement with the measured pattern. Even though the higher-order diffraction terms and the reflections inside the horn are neglected, the combination of the employed concepts and assumptions constitutes a new method of analysis for horn antennas. We shall follow this new method to develop a more complete analysis by including the previously neglected higher-order diffractions and the reflections inside the horn antenna.

## II. RADIATION MECHANISMS

The proposed antenna model is a corner reflector formed by two perfectly conducting plane walls intersecting at an angle,  $2\theta_E$ , as shown in Fig. 1. If we let the corner reflector be infinite in extent along the z-direction, the problem is thus reduced to a two-dimensional one. The primary source is a magnetic line current assumed at the vertex S. This assumption considerably simplifies treatment in the principal E-plane of a horn antenna fed by a waveguide supporting the  $TE_{10}$  mode.

The angular coordinate,  $\theta$ , shown in Fig. 1, is the common reference angle. The angles  $\psi$  are the diffraction angles referred to each individual wedge at which diffraction occurs. The angles  $\alpha$  are called incident angles of illumination. All the first subscripts refer to the points at which diffraction occurs, while the second subscripts refer to the points of origin of incident rays. This notation will be used throughout the following discussions. There are four wedges (A, B, S, and W) to be treated by diffraction theory. Wedges A and B have zero wedge angle, while wedges S and W have wedge angles of  $2\theta_E$  and  $2(\pi-\theta_E)$ , respectively. The property of symmetry of the reflector will be used to simplify the problem by considering only the upper half of the pattern.

In diffraction theory, a uniform cylindrical wave is radiated from the primary source in the region  $-\theta_E \leq \theta \leq \theta_E$ . This uniform cylindrical

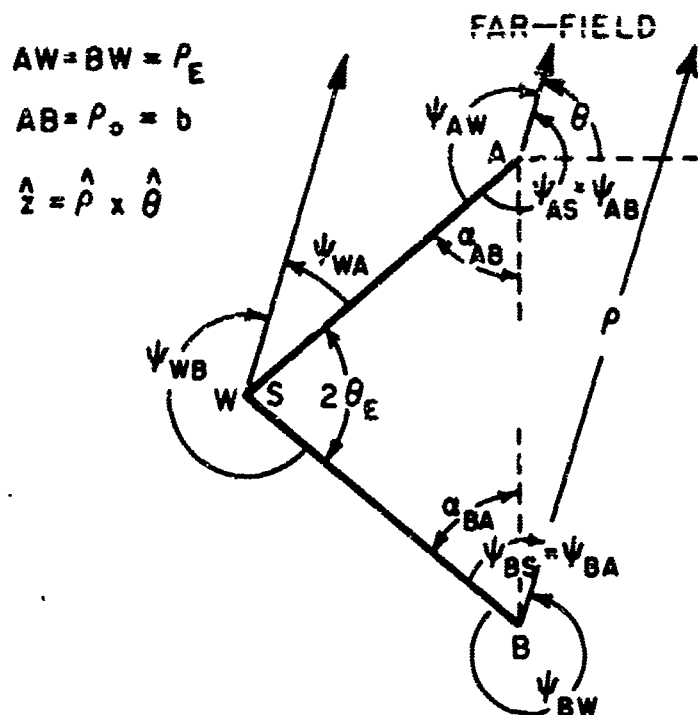


Fig. 1. Corner reflector.

wave is called the geometrical optics wave which illuminates wedges A and B. The diffractions at A and B caused by this illumination are called the first-order diffractions which have the solutions shown in Eq. (32) (Appendix A). The solutions are directional cylindrical waves radiated from the wedges. The geometrical optics rays from S and the first-order diffracted rays from A and B are shown in Fig. 2a. The first-order radiation pattern in the far-field can now be obtained by superposition of the far-field intensities of the primary source and the two induced sources.

To consider the diffraction process further, one can observe from Fig. 2b that the induced source at B illuminates wedges A, S, and W to give three second-order diffraction terms. In the same manner, the first-order-induced source at A illuminates wedges B, S, and W to give three more second-order diffracted waves. These six second-order-induced sources will continue to give third- and higher-order diffraction. The induced intensity becomes smaller with increasing order, and the phase delay of successive illumination can be properly taken into account.

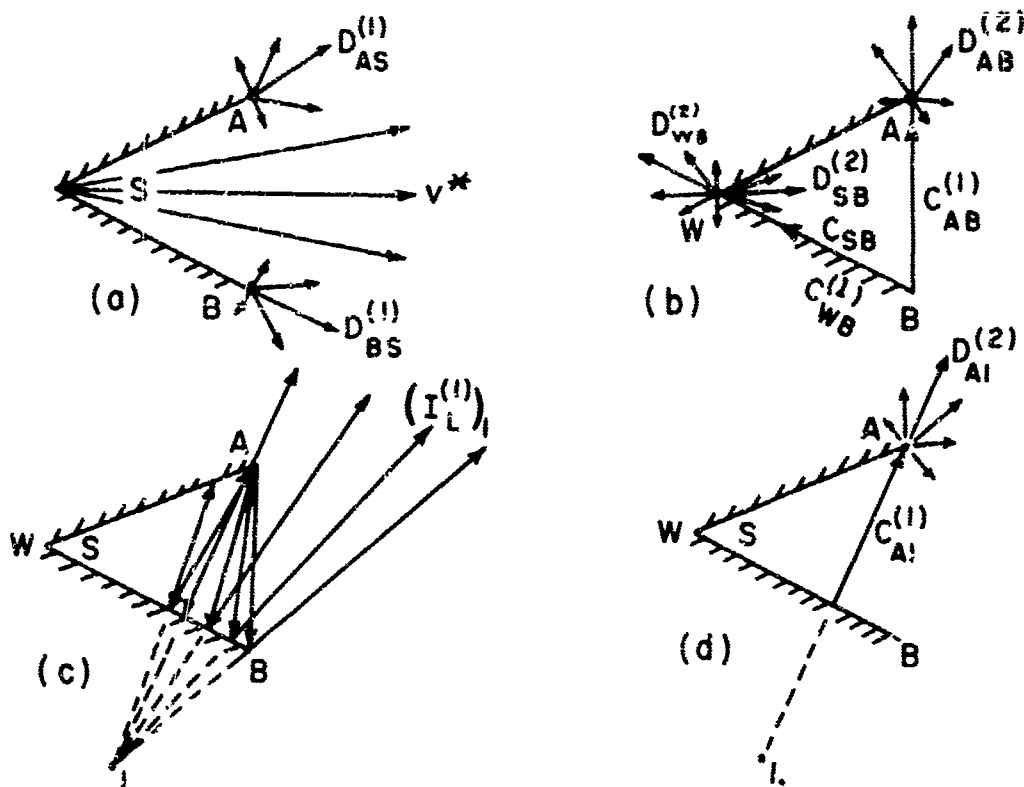


Fig. 2. Radiation mechanism of the antenna model. a) Direct rays and the 1st-order diffracted rays due to illumination from primary source at S; b) The 2nd-order diffractions due to the 1st-order illumination from B; c) The first image in the lower wall due to the 1st-order diffraction at A; and d) The 2nd-order diffraction due to the first image in the lower wall.

Since the reflector has perfectly conducting walls, the diffracted waves from A and B are reflected by the walls. The first-order diffracted rays from A are partially reflected by the lower wall, as shown in Fig. 2c. The reflected rays can be described by the image method of Appendix B. Figure 2d shows that wedge A is illuminated by one of the first-order images from the lower wall. The number of images is determined by the flare angle of the reflector. The effects of the reflector walls can then be taken into account by the images and the subsequent diffraction of the images.

When the process of diffraction and reflection described above is completed, the far-field patterns of the reflector antenna can be obtained by superimposing the contributions from the primary source at S; the induced sources at A, B, S, and W; and the images in both walls. Formulation of the pattern, including all orders of diffraction and reflection, is obtained in the next section.

### III. FORMULATION OF SOLUTION IN INFINITE SERIES FORM

Diffraction theory is briefly treated in Appendix A for both plane-wave and uniform cylindrical-wave illuminations. The wedges of the corner reflector studied here are all illuminated by cylindrical waves. In Appendix B, a method of images is presented to describe the image-waves formed inside the antenna. The diffraction theory and the method of images are used in the following to formulate a solution for our problem.

First, referring to Figs. 1 and 2a, the geometrical optics wave radiated from the primary source S is a uniform cylindrical-wave, defined as

$$(1) \quad v^*(\theta) = 1 \quad -\theta_E \leq \theta \leq +\theta_E,$$

where  $v^*$  has point S as phase-reference, and outside the defined region  $v^*$  is identically zero. The cylindrical-wave propagation factor  $R^{-\frac{1}{2}}$   $\text{Exp.}(-jkR)$  to the far-field is suppressed in Eq. (11) because only the angular dependence is of interest.

Wedges A and B are illuminated by the cylindrical wave from S with zero incident-angle. Since there is no reflection term, the diffracted waves from A and B have only one term of the solutions given by Eq. (32). Excluding the portion of waves diffracted into the corner reflector, the waves directly diffracted to the far-field can be written as

$$(2) \quad D_{AS}^{(1)} = v_B(\rho_E, \pi - \theta_E + \theta, 2) \quad -\frac{\pi}{2} \leq \theta \leq \pi + \theta_E,$$

$$D_{BS}^{(1)} = v_B(\rho_E, \pi - \theta_E - \theta, 2) \quad \frac{\pi}{2} \geq \theta \geq -(\pi + \theta_E),$$

$$\Phi_{AS} = \psi_{AS} = \pi - \theta_E + \theta,$$

$$\Phi_{BS} = \psi_{BS} = \pi - \theta_E - \theta,$$

$$(2) \quad \rho_E = SA = SB, \text{ and}$$

(cont)

$$n_A = n_B = 2,$$

where  $D_{AS}$  and  $D_{BS}$  designate diffraction at A and B because of illumination from S. The superscript (1) means first-order diffraction. The expressions of  $\phi$ 's in terms of  $\theta$  can be obtained from Fig. 1. The argument n is equal to 2 for both A and B because they have zero wedge angle. It should be noted that the notation  $v_B$  follows the form of the original solution and the subscript B has no connection with the wedge B.

The first-order radiation patterns, neglecting the reflections inside the corner reflector, can now be obtained by simply superimposing the terms in Eqs. (1) and (2). The discontinuities in  $V^*$  at  $\theta = \pm \theta_E$  in Eq. (1) are eliminated by  $D_{AS}^{(1)}$  and  $D_{BS}^{(1)}$ , respectively, in the manner illustrated in Eq. (34). Although the pattern is made continuous at  $\theta = \pm \theta_E$ , two sets of new discontinuities at  $\theta = \pm \pi/2$  and  $\pm(\pi + \theta_E)$  are observed in Eq. (2). Therefore, the first-order pattern in general has discontinuities at these directions.

Let us next examine the reflections of the first-order rays diffracted into the reflector. Since the diffracted waves from A and B are symmetrical with respect to  $\theta = 0$ , as can be seen from Eq. (2), the image-waves from the reflector can be treated as in Appendix B. The images are formed symmetrically in the lower and upper walls. Replacing  $\theta$  of  $D_{AS}^{(1)}$  and  $D_{BS}^{(1)}$  in Eq. (2) by  $(-2i\theta_E - \theta)$  and  $(2i\theta_E - \theta)$ , respectively, the image-waves from two walls can be obtained similar to Eq. (44) as

$$(3) \quad \begin{aligned} (I_L^{(1)})_i &= v_B(\rho_E, \pi - (2i+1)\theta_E - \theta, 2), \quad \frac{\pi}{2} - (i+1)\theta_E \leq \theta \leq \frac{\pi}{2} - i\theta_E; \\ (I_U^{(1)})_i &= v_B(\rho_E, \pi - (2i+1)\theta_E + \theta, 2), \quad -\left[\frac{\pi}{2} - (i+1)\theta_E\right] \geq \theta \geq -\left[\frac{\pi}{2} - i\theta_E\right]; \end{aligned}$$

$i = 1, 2, 3 \dots h$ ; and

$$h \text{ (the largest integer)} \leq \frac{\pi}{2\theta_E},$$

where the subscripts L and U indicate that the image terms are from the lower and the upper walls, respectively. The number of images in each wall is equal to  $h$ , as discussed in Appendix B. The division of regions is also studied in Appendix B. When the ratio  $\pi/2\theta_E$  is not an integer, the valid region for the last images should be modified to

$$(4) \quad \frac{\pi}{2} - (h+1)\theta_E \leq \theta \leq \pi - (2h+1)\theta_E \quad \text{for the lower-wall,}$$

and

$$-\left[\frac{\pi}{2} - (h+1)\theta_E\right] \geq \theta \geq -[\pi - (2h+1)\theta_E] \quad \text{for the upper-wall.}$$

Each term in Eq. (3) has its properly defined regions and is set zero outside the region. The first image in the lower wall, caused by the first-order-diffracted rays from A, is shown in Fig. 2c. Figure 3 shows the images in the lower wall for  $h = 4$ . It is noted that the true image waves of the diffracted waves from A are those with  $i$  odd in the lower wall and  $i$  even in the upper wall.

Descriptions of the first-order diffracted waves from A and B and their reflected waves have been completed above. The higher-order terms to be treated in the following discussion are necessary for cases in which small dimensions are encountered or high accuracy is desired. Physically, the higher-order terms describe the effects of illumination of edges by the lower-order-induced sources and their images. Mathematically, they are required to overcome the discontinuities of the lower-order terms in the radiation pattern. Taking the two first-order diffraction terms in Eq. (2), for instance, the discontinuities mentioned earlier can only be eliminated by taking into account the second-order diffraction in the specified directions.

At  $\theta = \pi/2$  in Eq. (2), wedge A is illuminated by the first-order-induced source at B. This intensity of illumination from B to A is called the first-order coupling coefficient,

$$C_{AB}^{(1)} = D_{BS}^{(1)} \left( \theta = \frac{\pi}{2} \right) ,$$

as shown in Fig. 2b. Because of symmetry, the first-order coupling coefficient from A to B in the direction  $\theta = -\pi/2$  is equal to  $C_{AB}^{(1)}$ . Therefore, using Eq. (2), we have

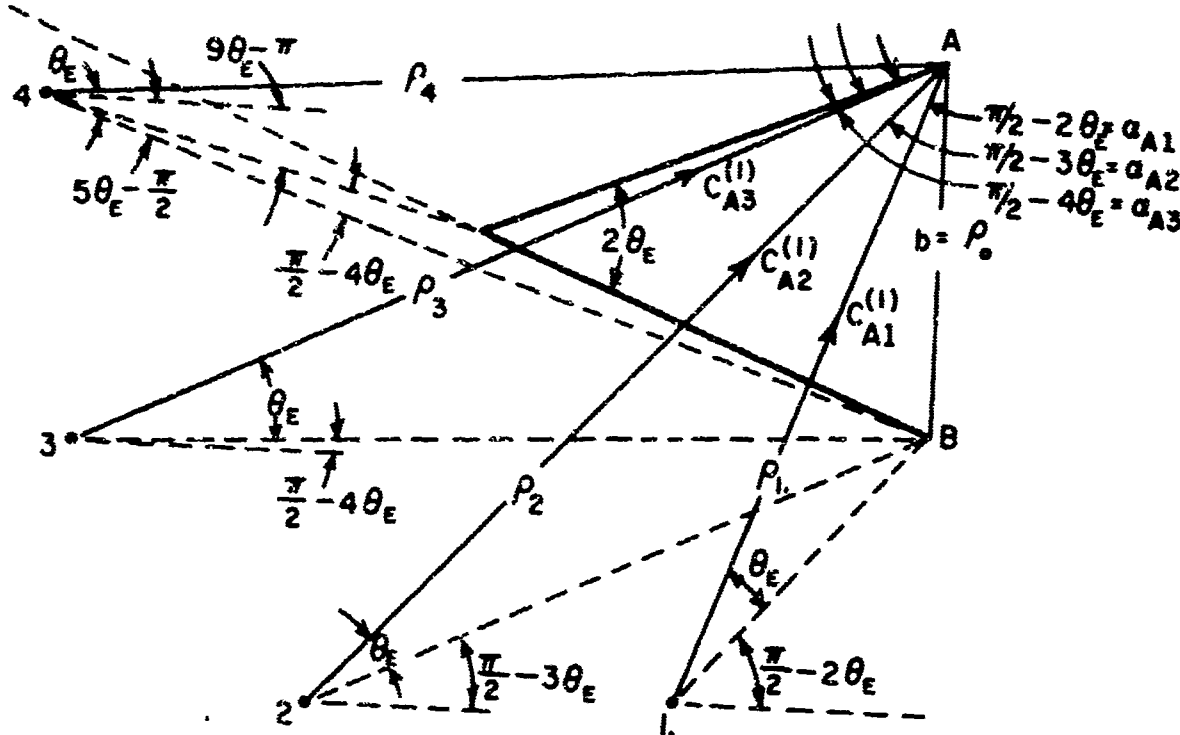


Fig. 3. Four images in the lower-wall.

$$(5) \quad C_{AB}^{(1)} = C_{BA}^{(1)} = v_B(\rho_E, \frac{\pi}{2} - \theta_E, 2).$$

Similarly, wedge W is illuminated by both A and B at  $\theta = \pm(\pi + \theta_E)$ , respectively. The coupling coefficients can be obtained in the same manner as

$$(6) \quad C_{WA}^{(1)} = C_{WB}^{(1)} = v_B(\rho_E, 2\pi, 2).$$

Since the diffracted waves are slowly varying functions in the neighborhood of a certain angle, it is a good approximation that wedges A, B, and W are illuminated by uniform cylindrical waves of the intensities shown in Eqs. (5) and (6). Under this assumption, the second-order diffracted waves can be obtained as

$$(7) \quad D_{AB}^{(2)} = C_{AB}^{(1)} \left[ v_B(b, \frac{\pi}{2} + \theta, z) + v_B(b, \frac{3\pi}{2} - 2\theta_E + \theta, z) \right],$$

$$-\frac{\pi}{2} \leq \theta \leq \pi + \theta_E;$$

$$D_{BA}^{(2)} = C_{BA}^{(1)} \left[ v_B(b, \frac{\pi}{2} - \theta, z) + v_B(b, \frac{3\pi}{2} - 2\theta_E - \theta, z) \right],$$

$$\frac{\pi}{2} \geq \theta \geq -(\pi + \theta_E);$$

$$D_{WA}^{(2)} = C_{WA}^{(1)} [v_B(p_E, -\theta_E + \theta, n_W)], \quad \theta_E \leq \theta \leq 2\pi - \theta_E; \text{ and}$$

$$D_{WB}^{(2)} = C_{WB}^{(1)} [v_B(p_E, 2\pi - \theta_E - \theta, n_W)], \quad -\theta_E \geq \theta \geq -(2\pi - \theta_E),$$

where the arguments used can be obtained from Fig. 1 as

$$(8) \quad \phi_{AB}^{\pm} = \psi_{AB} \mp \alpha_{AB} = (\pi - \theta_E + \theta) \mp (\frac{\pi}{2} - \theta_E),$$

$$\phi_{BA}^{\pm} = \psi_{BA} \mp \alpha_{BA} = (\pi - \theta_E - \theta) \mp (\frac{\pi}{2} - \theta_E),$$

$$\phi_{WA} = \psi_{WA} = \theta - \theta_E,$$

$$\phi_{WB} = \psi_{WB} = 2\pi - \theta_E - \theta,$$

$$n_W = 2 - \frac{2\theta_E}{\pi},$$

where  $n_W$  is obtained from wedge angle,  $(2-n_W)\pi$ , of wedge W. Next, we note in Eq. (3) that the image waves are discontinuous at angles

$$\theta = \pm (\frac{\pi}{2} - i\theta_E), \quad i = 1, 2, 3 \dots (h-1),$$

at which the wedges A and B are illuminated by the rays from images of lower and upper walls, respectively. Figure 3 shows the geometry of the images with  $h=4$  in the lower wall. The coupling coefficients from the images to wedge A can be obtained from Eqs. (3) as

$$C_{Ai}^{(1)} = \frac{I^{(1)}}{L} (\theta = \frac{\pi}{2} - i\theta_E), \quad i = 1, 2, \dots, (h-1).$$

By symmetry, the coupling coefficients from the images in the upper wall to wedge B are equal to  $C_{Bi}^{(1)}$  as

$$(9) \quad C_{Ai}^{(1)} = C_{Bi}^{(1)} = v_B(\rho_E, \frac{\pi}{2} - (i+1)\theta_E, 2), \quad i = 1, 2, \dots, (h-1).$$

The second-order diffraction at A and B illuminated by the images can now be written as

$$(10) \quad D_{Ai}^{(2)} = C_{Ai}^{(1)} \left[ v_B(\rho_i, \frac{\pi}{2} + i\theta_E + \theta, 2) + v_B(\rho_i, \frac{3\pi}{2} - (i+2)\theta_E + \theta, 2) \right],$$

$$-\frac{\pi}{2} \leq \theta \leq \pi + \theta_E,$$

$$D_{Bi}^{(2)} = C_{Bi}^{(1)} \left[ v_B(\rho_i, \frac{\pi}{2} + i\theta_E - \theta, 2) + v_B(\rho_i, \frac{3\pi}{2} - (i+2)\theta_E - \theta, 2) \right],$$

$$\frac{\pi}{2} \geq \theta \geq -(\pi + \theta_E),$$

and

$$i = 1, 2, \dots, (h-1),$$

where the arguments can be obtained by using Fig. 3 with  $h = 4$  as reference.

$$(11) \quad \phi_{Ai}^t = \psi_{AS} \mp \alpha_{Ai} = (\pi - \theta_E + \theta) \mp (\frac{\pi}{2} - (i+1)\theta_E),$$

$$\phi_{Bi}^t = \psi_{BS} \mp \alpha_{Bi} = (\pi - \theta_E - \theta) \mp (\frac{\pi}{2} - (i+1)\theta_E),$$

$$(11) \quad \rho_i = \rho_{i-1} \cos \theta_E + \rho_0 \cos i\theta_E, \text{ and}$$

(cont)

$$i = 1, 2, \dots, (h-1).$$

The second-order diffraction terms obtained in Eq. (10) are appropriately arranged for each boundary of the defined regions in Eq. (3), except that the last boundary is given by  $\theta = \pm (\pi/2 - (h+1)\theta_E)$  if  $\pi/2\theta_E$  is an integer, or  $\theta = \pm (\pi - (2h+1)\theta_E)$  if  $\pi/2\theta_E$  is not an integer. The boundaries in either case correspond to the directions in which wedge S is illuminated by the induced sources at A and B. Therefore, the coupling coefficients from A and B to S can be obtained from Eq. (3) by symmetry as

$$(12) \quad C_{SA}^{(1)} = C_{SB}^{(1)} = v_B(\rho_E, 0, 2),$$

which gives rise to the second-order diffraction at wedge S as

$$(13) \quad \left. \begin{aligned} D_{SA}^{(2)} &= C_{SA}^{(1)} [v_B(\rho_E, \theta_E - \theta, n_S)] \\ D_{SB}^{(2)} &= C_{SB}^{(1)} [v_B(\rho_E, \theta_E + \theta, n_S)] \end{aligned} \right\} \quad -\theta_E \leq \theta \leq +\theta_E, \\ \phi_{SA} = \theta_E - \theta, \\ \phi_{SB} = \theta_E + \theta, \text{ and} \\ n_S = 2 - n_W = \frac{2\theta_E}{\pi}. \end{math>$$

Now, we have completed the descriptions of all second-order diffractions which physically take into account the effects of illumination by the first-order-induced sources and mathematically eliminate all the first-order discontinuities. Summing up the second-order diffraction at A, B, W, and S gives

$$(14) \quad D_A^{(2)} = D_{AB}^{(2)} + \sum_{i=1}^{h-1} D_{Ai}^{(2)}, \quad -\frac{\pi}{2} \leq \theta \leq \pi + \theta_E;$$

$$(14) \quad \text{cont.} \quad D_B^{(2)} = D_{BA}^{(2)} + \sum_{i=1}^{h-1} D_{Bi}^{(2)}, \quad \frac{\pi}{2} \geq \theta \geq -(\pi + \theta_E);$$

$$D_W^{(2)} = D_{WA}^{(2)} + D_{WB}^{(2)}, \quad \theta_E \leq \theta \leq -\theta_E;$$

$$D_S^{(2)} = D_{SA}^{(2)} + D_{SB}^{(2)}, \quad -\theta_E \leq \theta \leq \theta_E,$$

where Eqs. (7), (10), and (13) can be used for computation. Following the same procedure used to obtain Eq. (3), the second-order image waves from the lower and upper walls can be obtained as

$$(15) \quad (I_L^{(2)})_i = C_{AB}^{(1)} \left[ v_B(b, \frac{\pi}{2} - 2i\theta_E - \theta, 2) + v_B(b, \frac{3\pi}{2} - 2(i+1)\theta_E - \theta, 2) \right]$$

$$+ \sum_{k=1}^{h-1} C_{Ak} \left[ v_B(p_k, \frac{\pi}{2} - i\theta_E - \theta, 2) + v_B(p_k, \frac{3\pi}{2} - (3i+2)\theta_E - \theta, 2) \right],$$

$$\frac{\pi}{2} - (i+1)\theta_E \leq \theta \leq \frac{\pi}{2} - i\theta_E;$$

$$(I_U^{(2)})_i = C_{BA}^{(1)} \left[ v_B(b, \frac{\pi}{2} - 2i\theta_E + \theta, 2) + v_B(b, \frac{3\pi}{2} - 2(i+1)\theta_E + \theta, 2) \right]$$

$$+ \sum_{k=1}^{h-1} C_{Bk} \left[ v_B(p_k, \frac{\pi}{2} - i\theta_E + \theta, 2) + v_B(p_k, \frac{3\pi}{2} - (3i+2)\theta_E + \theta, 2) \right],$$

$$-\left[ \frac{\pi}{2} - (i+1)\theta_E \right] \geq \theta \geq -\left[ \frac{\pi}{2} - i\theta_E \right];$$

and

$$i = 1, 2, 3, \dots, h,$$

where the  $\theta$  of  $D_A^{(2)}$  and  $D_B^{(2)}$  in Eq. (14) have been replaced by  $(\pm 2i\theta_E - \theta)$ , respectively. Note that the boundary of the last image  $i=h$  should follow Eq. (4), if  $\pi/2\theta_E$  is not exactly an integer.

We have observed above that while the first-order discontinuities are eliminated by the inclusion of second-order diffractions, new discontinuities occur again at the boundaries of the regions defined in Eqs. (14) and (15). These second-order discontinuities can be eliminated only by introducing third-order diffraction. The higher the order of diffraction the smaller will be the magnitude of discontinuities. It is theoretically possible to consider the order of diffraction as high as desired. In other words, magnitude of discontinuities can be made negligibly small if sufficient order of diffraction is included.

For completeness, let us consider higher-order diffraction. The third-order diffraction at wedge A is caused not only by illuminations from the second-order-induced sources at B and the images in the lower wall, but also by illumination from wedges W and S. In the same manner as Eq. (14), the resultant third-order diffraction at A can be obtained as

$$D_A^{(3)} = D_{AB}^{(3)} + D_{AW}^{(3)} + D_{AS}^{(3)} + \sum_{i=1}^{h-1} D_{Ai}^{(3)}.$$

Similarly, by including all the  $(m-1)^{\text{th}}$ -order-induced sources and images, the  $m^{\text{th}}$ -order diffraction at wedges A, B, W, and S and the images of the corner reflector can be summarized as

$$(16) \quad D_A^{(m)} = D_{AB}^{(m)} + D_{AW}^{(m)} + D_{AS}^{(m)} + \sum_{i=1}^{h-1} D_{Ai}^{(m)},$$

$$D_B^{(m)} = D_{BA}^{(m)} + D_{BW}^{(m)} + D_{BS}^{(m)} + \sum_{i=1}^{h-1} D_{Bi}^{(m)},$$

$$D_W^{(m)} = D_{WA}^{(m)} + D_{WB}^{(m)},$$

$$D_S^{(m)} = D_{SA}^{(m)} + D_{SB}^{(m)},$$

$$(16) \quad \text{cont.} \quad (I_L^{(m)})_i = D_A^{(m)} (\theta = -2i\theta_E - \theta), \text{ and}$$

$$(I_U^{(m)})_i = D_B^{(m)} (\theta = +2i\theta_E - \theta),$$

where the valid regions are identical to those defined in Eqs. (14) and (15). The components in Eq. (16) can be obtained analogous to Eqs. (7), (10), and (13) as follows (the equal sign following  $\theta$  in the parentheses means "replaced by");

$$(17) \quad D_{AB}^{(m)} = C_{AB}^{(m-1)} [v_B(b, \frac{\pi}{2} + \theta, 2) + v_B(b, \frac{3\pi}{2} - 2\theta_E + \theta, 2)],$$

$$-\frac{\pi}{2} \leq \theta \leq \pi + \theta_E;$$

$$D_{BA}^{(m)} = D_{AB}^{(m)} (\theta = -\theta), \quad \frac{\pi}{2} \geq \theta \geq -(\pi + \theta_E);$$

$$D_{WA}^{(m)} = C_{WA}^{(m-1)} [v_B(p_E, -\theta_E + \theta, n_W)], \quad \theta_E \leq \theta \leq 2\pi - \theta_E;$$

$$D_{WB}^{(m)} = C_{WA}^{(m-1)} [v_B(p_E, 2\pi - \theta_E - \theta, n_W)], \quad -\theta_E \geq \theta \geq -(2\pi - \theta_E);$$

$$\left. \begin{aligned} D_{SA}^{(m)} &= C_{SA}^{(m-1)} [v_B(p_E, \theta_E - \theta, n_S)] \\ D_{SB}^{(m)} &= D_{SA}^{(m)} (\theta = -\theta) \end{aligned} \right\} -\theta_E \leq \theta \leq \theta_E;$$

$$D_{Ai}^{(m)} = C_{Ai}^{(m-1)} [v_B(p_i, \frac{\pi}{2} + i\theta_E + \theta, 2) + v_B(p_i, \frac{3\pi}{2} - (i+2)\theta_E + \theta, 2)],$$

$$-\frac{\pi}{2} \leq \theta \leq \pi + \theta_E;$$

$$D_{Bi}^{(m)} = D_{Ai}^{(m)} (\theta = -\theta), \quad \frac{\pi}{2} \geq \theta \geq -(\pi + \theta_E);$$

$$D_{AW}^{(m)} = C_{AW}^{(m-1)} [v_B(p_E, \pi + \theta_E - \theta, 2)], \quad -\frac{\pi}{2} \leq \theta \leq \pi + \theta_E;$$

$$D_{BW}^{(m)} = D_{AW}^{(m)} (\theta = -\theta), \quad \frac{\pi}{2} \geq \theta \geq -(\pi + \theta_E);$$

$$(17) \quad \text{cont.} \quad D_{AS}^{(m)} = C_{AS}^{(m-1)} [v_B(\rho_E, \pi - \theta_E + \theta, 2)], \quad -\frac{\pi}{2} \leq \theta \leq \pi + \theta_E;$$

and

$$D_{BS}^{(m)} = D_{AS}^{(m)}(\theta = -\theta), \quad \frac{\pi}{2} \geq \theta \geq -(\pi + \theta_E),$$

where the property of symmetry with respect to  $\theta = 0$  is used to obtain symmetrical terms. The coupling coefficients of different orders are obtained in Appendix C. As soon as coupling coefficients are properly evaluated, the diffraction of any order can then be obtained by making use of Eqs. (16) and (17).

Finally, the total far-field pattern of the corner reflector can now be obtained by superposition of all terms presented above. Taking wedge A as a common phase reference, and considering only the upper-half region,  $0 \leq \theta \leq \pi$ , the total far-field  $u(\theta)$  can be written in a form similar to Eq. (46) as

$$(18) \quad u(\theta) = \left[ v^* + \sum_{m=2}^{\infty} D_S^{(m)} \right] y_{AS} + \left[ \sum_{m=1}^{\infty} D_A^{(m)} \right] + \left[ \sum_{m=1}^{\infty} D_B^{(m)} \right] y_{AB}$$

$$+ \left[ \sum_{m=2}^{\infty} D_W^{(m)} \right] y_{AW} + \sum_{i=1}^h \left[ \sum_{m=1}^{\infty} (I_L^{(m)})_i \right] y_{Ai}$$

$$+ \left[ \sum_{m=1}^{\infty} (I_U^{(m)})_h \right] y_{Bh} y_{AB},$$

where the last images in the upper wall are included because in general they may contribute to the upper-half region. The local phase factors referred to A can be written from Figs. 1 and 3 as

$$(19) \quad y_{AS} = \text{Exp.} [-j2\pi \rho_E \cos(-\theta_E + \theta)],$$

$$y_{AB} = \text{Exp.} [-j2\pi b \sin \theta],$$

$$y_{AW} = \text{Exp.} \{ -j2\pi\rho_E \cos (\theta_E - \theta) \} = y_{AS},$$

$$y_{Ai} = \text{Exp.} \{ -j2\pi\rho_i \sin (i\theta_E + \theta) \},$$

and

$$y_{Bh} = \text{Exp.} \{ -j2\pi\rho_i \sin (h\theta_E - \theta) \}.$$

#### IV. THE APPROXIMATED SOLUTIONS

The pattern of the corner reflector in Fig. 1 can be calculated by Eqs. (18) and (19) as accurately as desired. Since the contributions of the higher-order terms to the pattern decrease with increasing order, computation can be made by including only those terms which are significant in their defined regions. The following approximations are made to obtain a pattern including only significant higher-order terms.

First, referring to Fig. 2a, the contributions from wedge S are the geometrical optics term  $v^*$  of Eq. (1) due to the primary source, and the diffracted terms  $D_S^{(m)}$  due to the induced sources. The lowest-order diffracted terms are due to the second-order-induced sources. Therefore, the most significant contribution from the diffracted terms is  $D_S^{(2)}$ , given in Eq. (14). Computation of the illumination intensity,  $C_{SA}^{(1)}$ , indicates that for typical dimensions the magnitude of  $D_S^{(2)}$  is generally very small compared to the unit intensity of  $v^*$ . Neglecting the diffracted terms, the contribution from wedge S may be approximated as

$$(20) \quad v^* + \sum_{m=2}^{\infty} D_S^{(m)} \approx v^* = 1, \quad 0 \leq \theta \leq \theta_E,$$

where the region of contribution is defined as such because only the upper-half region  $0 \leq \theta \leq \pi$  is under consideration.

Next, consider the contributions from the induced sources at A. The third- and higher-order terms of a typical reflector are also generally very small compared to unity. Therefore, the diffracted fields from A can be approximated by considering only  $D_{AS}^{(1)}$  and  $D_A^{(2)}$  in Eqs. (2) and (14), respectively. The diffracted fields from B can be approximated in the same manner. We thus have

$$(21) \quad \sum_{m=1}^{\infty} D_A^{(m)} \approx D_{AS}^{(1)} + D_{AB}^{(2)} + \sum_{i=1}^{h-1} D_{Ai}^{(2)}, \quad 0 \leq \theta \leq \pi,$$

and

$$\sum_{m=1}^{\infty} D_B^{(m)} \approx D_{BS}^{(1)} + D_{BA}^{(2)} + \sum_{i=1}^{h-1} D_{Bi}^{(2)}, \quad 0 \leq \theta \leq \frac{\pi}{2},$$

$$-(\pi + \theta_E) \leq \theta \leq \pi$$

The lowest-order contributions from the induced sources at wedges W and S are  $D_W^{(2)}$  and  $D_S^{(2)}$  which are also very small compared to the unit intensity of  $v^*$ . Since  $D_S^{(2)}$  is defined in the same region as  $v^*$ , the contribution from  $D_S^{(2)}$  to the total pattern can be neglected. But,  $D_W^{(2)}$  is defined outside the region of  $v^*$ ; therefore, in order to accurately calculate the side and back radiations in the pattern, we must at least approximate the contribution from W as

$$(22) \quad \sum_{m=2}^{\infty} D_W^{(m)} \approx D_{WA}^{(2)} + D_{WB}^{(2)}, \quad \theta_E \leq \theta \leq \pi.$$

As for contributions from the image terms, the magnitude, in general, decreases with increasing value of i. In other words, in the region of contribution,  $0 \leq \theta \leq \pi/2 - \theta_E$ , shown in Fig. 3, the images contribute to the total pattern more significantly in the upper end than in the lower end of the region. Therefore, in theory, approximation on the images should be made individually. But, we shall approximate images of the same order as a group so that all the images of the same order can be completely included. Assuming that the second- and higher-order images have negligible contribution to the total pattern, the image terms are approximated as

$$(23) \quad \sum_{m=1}^{\infty} (I_L^{(m)})_i \approx (I_L^{(1)})_i, \quad \frac{\pi}{2} - (i+1)\theta_E \leq \theta \leq \frac{\pi}{2} - i\theta_E.$$

An approximate pattern of the corner reflector can now be obtained from Eq. (18) by using Eqs. (19) to (23), as follows:

$$\begin{aligned}
 (24) \quad u(\theta) \approx & [v^*] y_{AS} + [D_{AS}^{(1)} + D_{AB}^{(2)} + \sum_{i=1}^{h-1} D_{Ai}^{(2)}] \\
 & + [D_{BS}^{(1)} + D_{BA}^{(2)} + \sum_{i=1}^{h-1} D_{Bi}^{(2)}] y_{AB} \\
 & + [D_{WA}^{(2)} + D_{WB}^{(2)}] y_{AW} \\
 & + \sum_{i=1}^h [I_L^{(1)}]_i y_{Ai} + [(I_U^{(1)})_h] y_{Bh} y_{AB} .
 \end{aligned}$$

Since this is an approximated pattern, discontinuities are expected to be increasingly noticeable with decreasing size of the corner reflector. Let us examine, term by term, the continuity of Eq. (24) in the upper-half region,  $0 \leq \theta \leq \pi$ . At  $\theta = \theta_E$ , the discontinuity of  $v^*$  in Eq. (20) is eliminated by  $D_{AS}^{(1)}$ . At  $\theta = \pi/2$ , the discontinuity of  $D_{BS}^{(1)}$  in Eq. (21) is eliminated by  $D_{AB}^{(2)}$ ; but there are no higher-order terms included in Eq. (24) to compensate for the discontinuities of  $D_{BA}^{(2)}$  and  $D_{Bi}^{(2)}$ , with  $i = 1, 2, \dots, (h-1)$ . Similarly, at  $\theta = -(\pi + \theta_E)$ , the discontinuity of  $D_{BS}^{(1)}$  is eliminated by  $D_{WB}^{(2)}$ , but those of  $D_{BA}^{(2)}$  and  $D_{Bi}^{(2)}$ , with  $i = 1, 2, \dots, (h-1)$ , are left uncompensated. The discontinuities at  $\theta = \pi/2 - i\theta_E$  of  $(I_L^{(1)})_i$  are all eliminated by  $D_{Ai}^{(2)}$  and  $D_{Bi}^{(2)}$ , with  $i = 1, 2, \dots, (h-1)$ . The discontinuity of  $(I_U^{(1)})_h$  takes place in the defined regions of  $v^*$  and is usually unnoticeably small. The discontinuities of  $D_{WA}^{(2)}$  and  $D_{WB}^{(2)}$  at  $\theta = \theta_E$  are also unnoticeably small for a typical corner reflector.

Within the accuracy of the approximations made to obtain Eq. (24), it is desirable to have the pattern continuous in the entire region. To accomplish this, the second-order discontinuities at  $\theta = \pi/2$  and  $-(\pi + \theta_E)$

mentioned above need to be eliminated. The coupling coefficients from B to A resulting from the second-order-induced sources at B can be obtained from Eq. (14) as

$$\begin{aligned}
 (25) \quad C_{AB}^{(2)} &= D_B^{(2)} \left( \theta = \frac{\pi}{2} \right), \\
 &= C_{BA}^{(1)} [v_B(b, 0, 2) + v_B(b, \pi - 2\theta_E, 2)] \\
 &+ \sum_{i=1}^{h-1} C_{Bi}^{(1)} [v_B(\rho_i, i\theta_E, 2) + v_B(\rho_i, \pi - (i+2)\theta_E, 2)], \\
 &= C_{BA}^{(1)} C_{ABA} + \sum_{i=1}^{h-1} C_{Bi}^{(1)} C_{ABi} \\
 &= C_{AB}^{(1)} C_{ABA} + \sum_{i=1}^{h-1} C_{Ai}^{(1)} C_{ABi},
 \end{aligned}$$

where Eqs. (9) and (10) are used and property of symmetry is employed for the first-order coupling coefficients. By symmetry, the second-order coupling coefficient from A to B can also be obtained from Eqs. (14), (7), and (10) as

$$C_{BA}^{(2)} = D_A^{(2)} \left( \theta = -\frac{\pi}{2} \right) = C_{AB}^{(2)}.$$

Because of the interaction between A and B by  $C_{AB}^{(2)}$ , a third-order diffraction can be written for A and B with the same defined region in Eq. (14). If the process of interaction between A and B continues to infinite order, a coupling coefficient can be obtained in closed form as

$$(26) \quad C_{AB} = \frac{C_{AB}^{(1)} + \sum_{i=1}^{h-1} C_{Ai}^{(1)} C_{ABi}}{1 - C_{ABA}}.$$

where  $C_{ABA}$  and  $C_{ABi}$  can be obtained from Eq. (25). The continuity of the total pattern at  $\theta = \pi/2$  is now ensured by using  $C_{AB}$  instead of  $C_{AB}^{(1)}$  for  $D_{AB}^{(2)}$  and  $D_{BA}^{(2)}$  in Eq. (24) as

$$(27) \quad D_{AB} = C_{AB} [v_B(b, \frac{\pi}{2} + \theta, 2) + v_B(b, \frac{3\pi}{2} - 2\theta_E + \theta, 2)], \quad 0 \leq \theta \leq \pi,$$

and

$$D_{BA} = C_{AB} [v_B(b, \frac{\pi}{2} - \theta, 2) + v_B(b, \frac{3\pi}{2} - 2\theta_E - \theta, 2)], \quad \begin{cases} 0 \leq \theta \leq \frac{\pi}{2} \\ -(\pi + \theta_E) \leq \theta \leq \pi, \end{cases}$$

where Eq. (7) is used and the regions are restricted to the upper-half region.

As a consequence of the modified equations in Eq. (27), the uncompensated terms at  $\theta = -(\pi + \theta_E)$  are now  $D_{BA}^{(2)}$  and  $D_{Bi}^{(2)}$ , with  $i = 1, 2, \dots, (h-1)$ . The coupling coefficient from B to W resulting from these terms can be written from Eqs. (27) and (10) as

$$\begin{aligned} C'_{WB} &= D_{BA}(\theta = -(\pi + \theta_E)) + \sum_{i=1}^{h-1} D_{Bi}^{(2)}(\theta = -(\pi + \theta_E)), \\ C'_{WA} &= D_{AB}(\theta = \pi + \theta_E) + \sum_{i=1}^{h-1} D_{Ai}^{(2)}(\theta = \pi + \theta_E) \\ &= C_{AB} [v_B(b, \frac{3\pi}{2} + \theta_E, 2) + v_B(b, \frac{5\pi}{2} - \theta_E, 2)] \\ &\quad + \sum_{i=1}^{h-1} C_{Ai}^{(1)} [v_B(p_i, \frac{3\pi}{2} + (i+1)\theta_E, 2) + v_B(p_i, \frac{5\pi}{2} - (i+1)\theta_E, 2)], \end{aligned}$$

which is a new coupling coefficient to ensure the continuity of the total pattern at  $\theta = -(\pi + \theta_E)$  or  $\pi - \theta_E$ . Adding this new coupling coefficient to  $C_{WA}^{(1)}$  in Eq. (7), the diffracted fields at W are modified as

$$(28) \quad \left. \begin{aligned} D_{WA} &= C_{WA} [v_B(\rho_E, -\theta_E + \theta, n_W)] \\ D_{WB} &= C_{WA} [v_B(\rho_E, 2\pi - \theta_E - \theta, n_W)] \end{aligned} \right\}, \quad \theta_E \leq \theta \leq \pi,$$

where

$$C_{WA} = C_{WA}^{(1)} + C_{WA}^{(2)}.$$

Using Eqs. (27) and (28), an approximated "continuous" pattern can be finally written from Eq. (24) as

$$(29) \quad u(\theta) = [v^*] y_{AS} + [D_{AS}^{(1)} + D_{AB} + \sum_{i=1}^{h-1} D_{Ai}^{(2)}] \\ + [D_{BS}^{(1)} + D_{BA} + \sum_{i=1}^{h-1} D_{Bi}^{(2)}] y_{AB} \\ + [D_{AW} + D_{BW}] y_{AW} \\ + \sum_{i=1}^h [(I_L^{(1)})_i y_{Ai} + (I_U^{(1)})_i y_{Bb} y_{AB}].$$

For typical dimensions of a corner reflector, Eq. (29) in general gives excellent prediction of the radiation pattern. Examples are given in the following section.

#### V. COMPUTED PATTERNS COMPARED WITH MEASURED PATTERNS OF HORN ANTENNAS

To illustrate the validity of the corner reflector as a model of the pyramidal horn antenna fed by a waveguide supporting  $TE_{10}$  mode, Eq. (29) is computed and compared with measured patterns. Figure 4 shows the experimental set-up of a horn antenna in which the idealized model is the corner reflector ASB used to derive Eq. (29). The associated

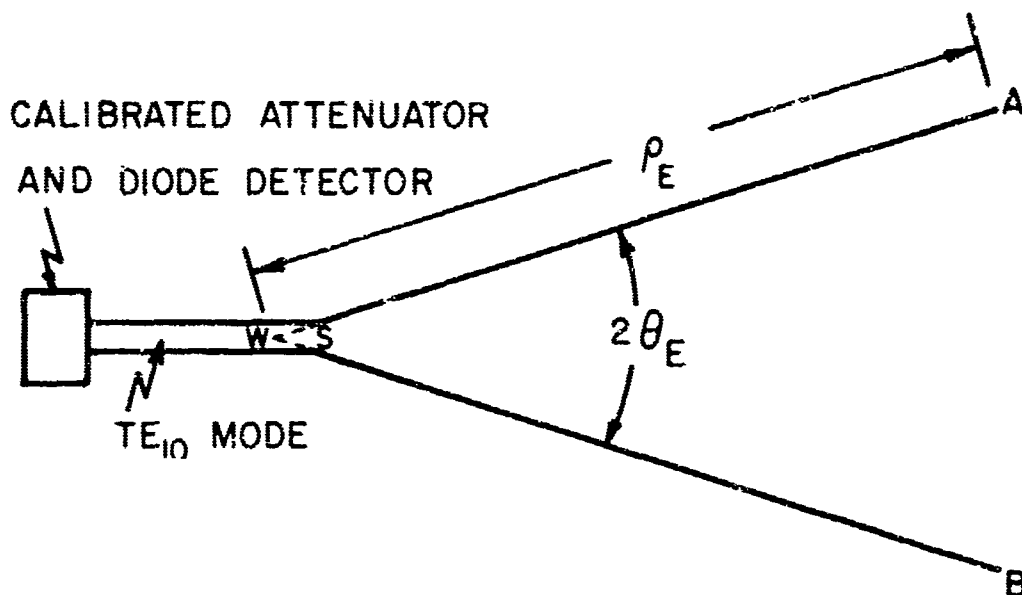


Fig. 4. The E-plane of a horn antenna.

waveguide and the calibrated attenuator and diode detector are not considered in pattern prediction.

First, consider a horn antenna of  $p_E = 41.3$  cm and  $2\theta_E = 35^\circ$  fed by a waveguide propagating the  $TE_{10}$  mode at 9.8 gc. The horn length,  $p_E$ , in terms of wavelength is equal to  $13.5\lambda$ . The measured far-field pattern is shown in Fig. 5. The pattern computed by Eq.(29) is shown displaced 5 db below the measured pattern. Comparison of two patterns shows excellent agreement in the overall lobe structure. The small deviation of relative field intensity in the region  $50^\circ < \theta < 80^\circ$  is primarily due to the approximation assumed in Eq. (23) that the second- and higher-order images are negligible. The presence of the waveguide and the associated attenuator and detector shown in Fig. 4 is responsible for the interference in the region  $80^\circ < \theta < 180^\circ$  of the measured pattern. In the process of computation, special care is required for the properly defined regions of each term in Eq. (29). Attention is also needed for the boundaries  $\theta = \theta_E$ ,  $90^\circ$ ,  $(90^\circ - \theta_E)$ , and  $(180^\circ - \theta_E)$  at which discontinuities are eliminated by higher-order terms. For convenience, the pattern computed by only first-order diffraction treated in Ref. 5 is plotted displaced 5 db above the measured pattern. As mentioned earlier, the discontinuities at  $\theta = 90^\circ$  and  $(180^\circ - \theta_E)$  are expected in the first-order pattern.

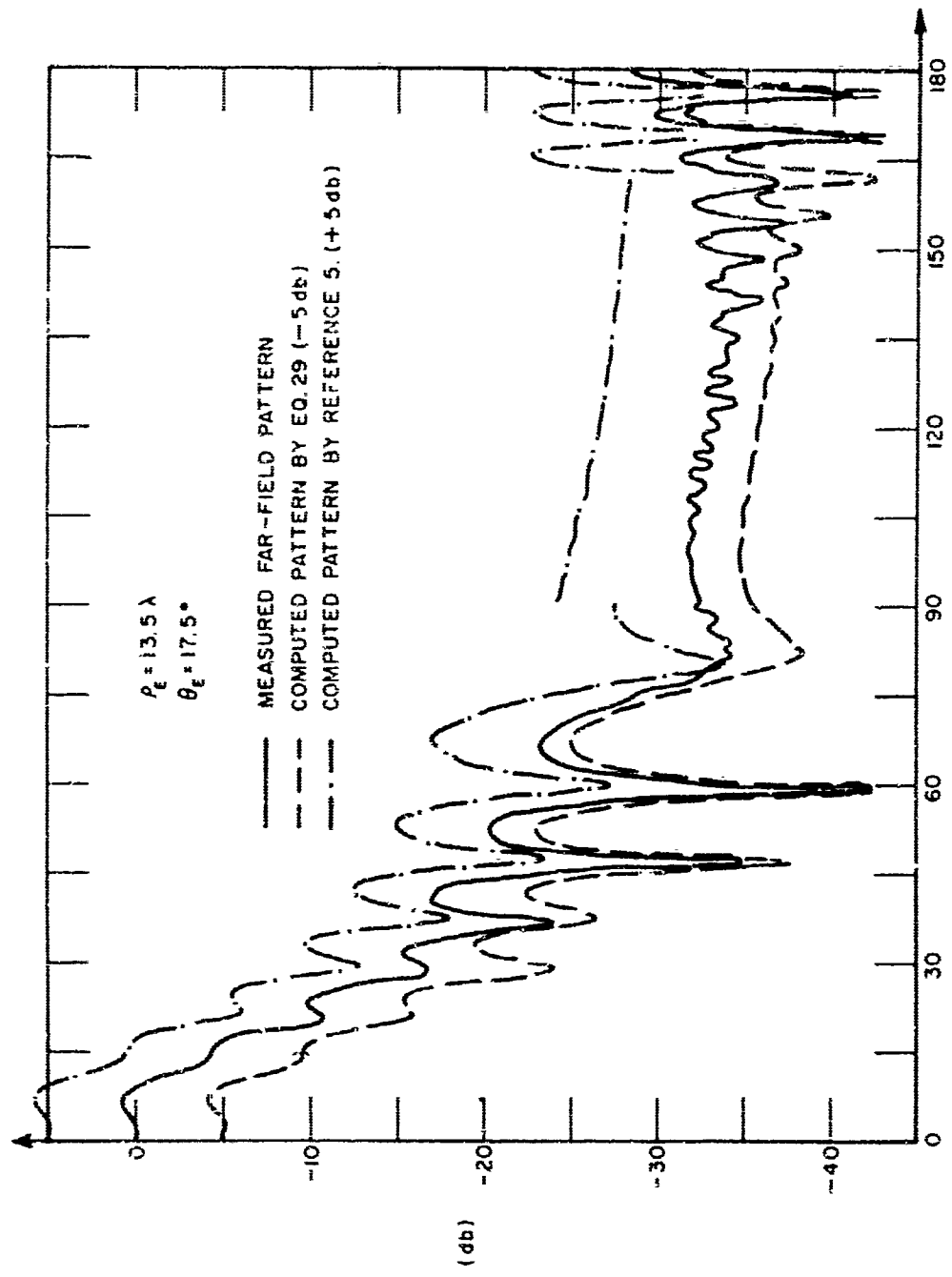


Fig. 5. A comparison of the patterns.

When the frequency is increased corresponding to  $\rho_E = 24.8\lambda$  for the same horn, the three patterns are as shown in Fig. 6. The same conclusions drawn for Fig. 5 remain true, except that the interference from the waveguide and the associated structure becomes larger because the physical size is larger in terms of wavelength. In Fig. 7, three patterns are shown for a small horn antenna of  $\rho_E = 5.61\lambda$  and  $\theta_E = 21.2^\circ$ . Although the overall lobe structure is still in good agreement with the measured pattern, a larger deviation in intensity level is observed around  $\theta = 80^\circ$  of the pattern by Eq. (29). This disagreement results because the second-order image terms neglected in Eq. (23) are not negligibly small for small horns. Therefore, better patterns can be obtained for small horns by including the second-order image terms and their subsequent effects on the total pattern.

The three examples presented above have demonstrated the accuracy of Eq. (29) for pattern computations of typical horn antennas. The accuracy of the experimental measurements is assumed to have 1 db fluctuation when the intensity is around 40 db below the reference intensity. In view of this, Eq. (29) is sufficient for horn antennas of typical dimensions. When  $\rho_E$  and  $\theta_E$  become smaller, it is easily observed from Fig. 7 that the second-order image terms in Eq. (15) should be included to ensure good prediction around the region  $\theta = 90^\circ - \theta_E$ .

## VI. RELATIVE BACK LEVELS

The radiation patterns, either measured or computed, always have a back-lobe maximum at  $\theta = 180^\circ$ , even though this maximum value is not necessarily the largest maximum in the region  $180^\circ - \theta_E < \theta < 180^\circ$ . In Fig. 6, for instance, the largest maximum value in the region is at  $176^\circ$  of the measured pattern and at  $\theta = 172.5^\circ$  of the computed patterns, using Eq. (29). This discrepancy results from the interference from the experimental set up which is not considered in the idealized reflector model. The difference between the value at  $\theta = 180^\circ$  and that of the largest maximum is generally small. Therefore, the radiation intensity at  $\theta = 180^\circ$  can be taken as a representative value for back-lobe region. It is also observed that the radiation intensity in the region  $90^\circ < \theta < 180^\circ - \theta_E$  is, in general, smaller than the mentioned representative value.

In EMC problems, it may be desirable to keep the pattern level in the region  $90^\circ < \theta < 180^\circ$  as low as possible. To predict a representative interference-intensity in this region, one can simply take the first-order diffraction terms in Eq. (2) for approximate computation. Neglecting all

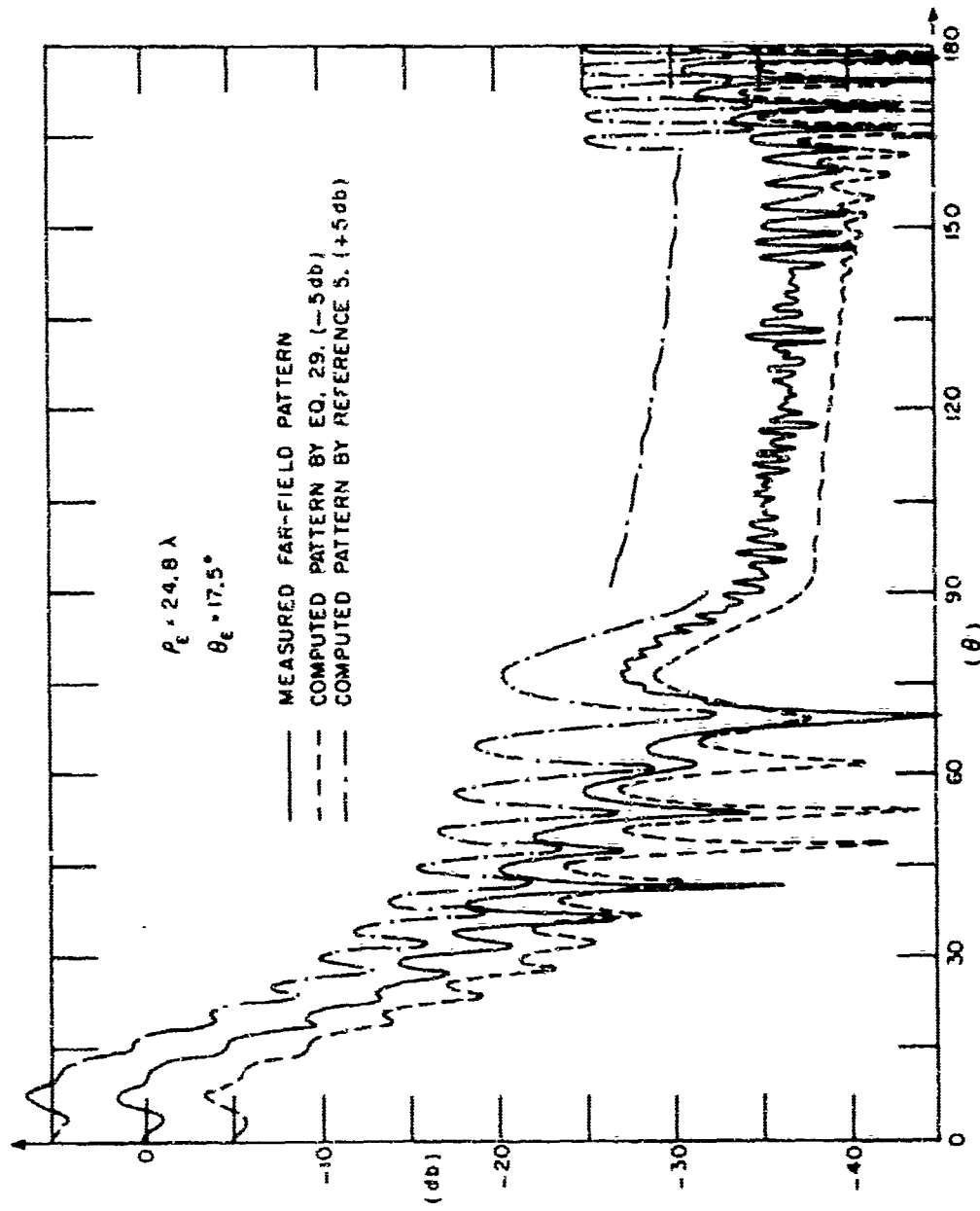


Fig. 6. Comparison of patterns.

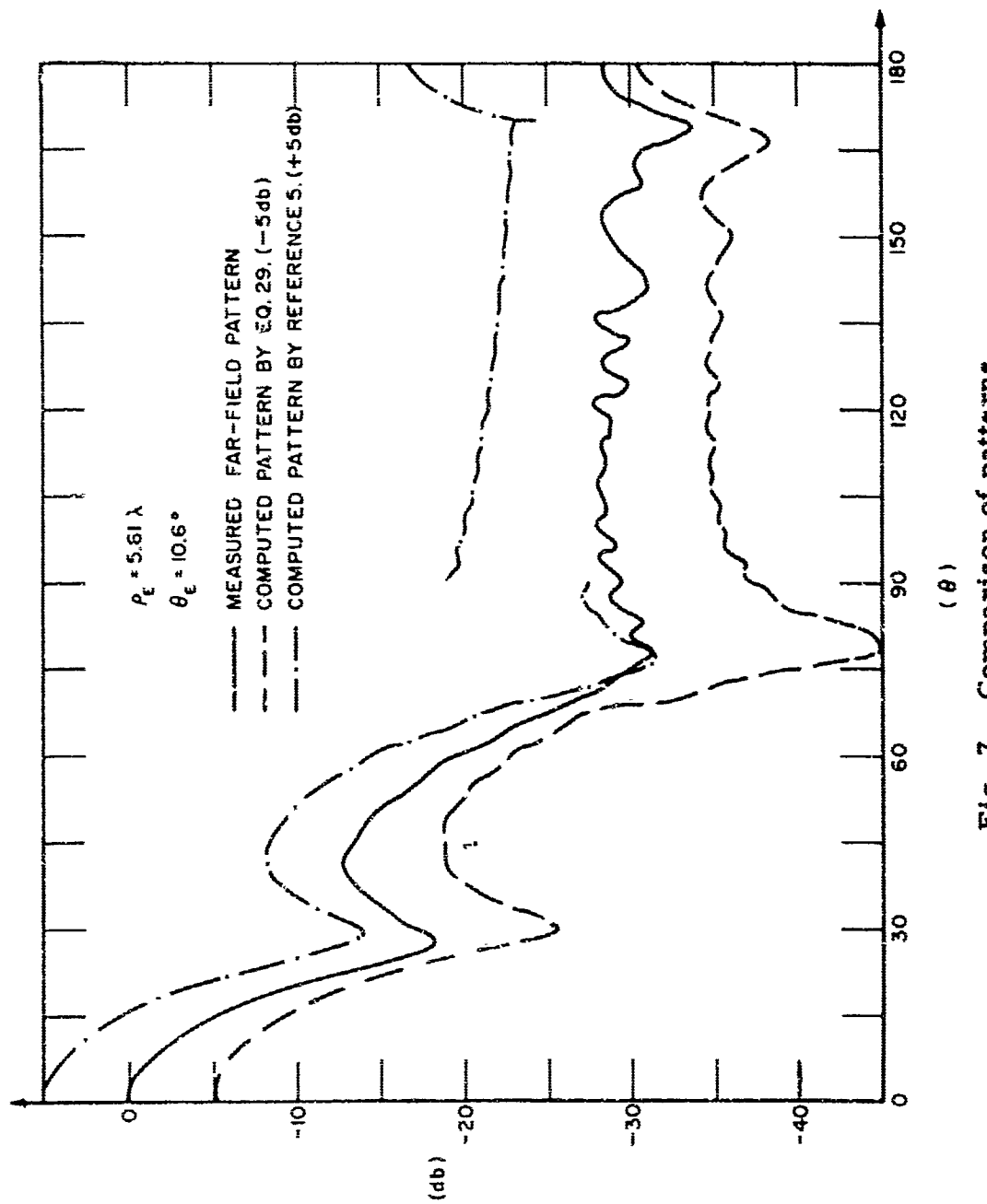


Fig. 7. Comparison of patterns.

higher-order terms, the radiation intensity at  $\theta = 180^\circ$  is given approximately by

$$u(\pi) = D_{AS}^{(1)}(\theta=\pi) + D_{BS}^{(1)}(\theta=-\pi)$$

$$= 2 v_B(\rho_E, 2\pi - \theta_E, 2).$$

The radiation intensity at  $\theta = 0^\circ$  is also approximated as

$$u(0) = Y_{AS}(\theta=0) + D_{AS}^{(1)}(\theta=0) + D_{BS}^{(1)}(\theta=0)$$

$$= \text{Exp}[-j2\pi \rho_E \cos \theta_E] + 2 v_B(\rho_E, \pi - \theta_E, 2).$$

where Eqs. (19) and (2) are used. The back-to-front ratio can then be obtained by plotting

$$20 \log \frac{|u(\pi)|}{|u(0)|},$$

which has only two parameters,  $\theta_E$  and  $\rho_E$ . For a horn antenna of fixed angle  $\theta_E$ , the back-to-front ratio can be plotted as a function  $\rho_E$ . Figure 8 shows seven curves for different horn dimensions to demonstrate that Fig. 8 can be used for approximate prediction of typical horn antennas. Fig. 9 gives a set of measured data for  $2\theta_E = 35^\circ$ . The data are taken from nine complete patterns of the antenna. The accuracy of prediction depends on both the approximation in computation and the equipment used in measurement. In general, it is expected that the larger the sizes of antenna the better the prediction.

It is interesting to compare the first minimum points in Fig. 8 to the defined optimum[6] horn lengths. The values of optimum horn lengths are tabulated in Fig. 8 and are found to be one half of that of  $\rho_E$ , which give the first minimum back-to-front ratios.

The sets of  $\rho_E$  and  $\theta_E$  giving rise to the minima in the curves do not necessarily imply that  $u(0)$  is maximum and that  $u(\pi)$  is minimum. The reason for this is the main lobe of pattern begins to bifurcate at the

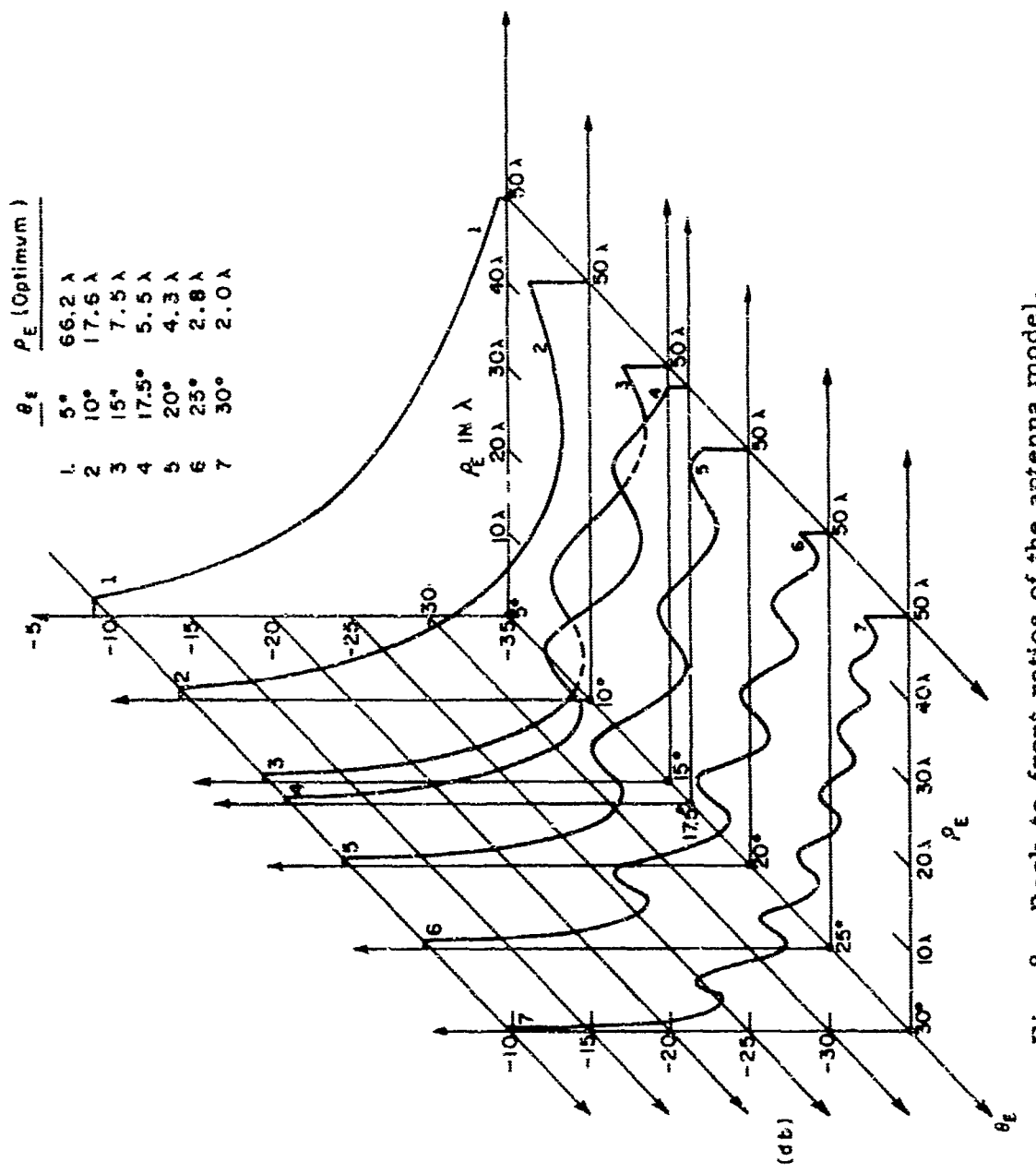


Fig. 8. Back-to-front ratios of the antenna model.

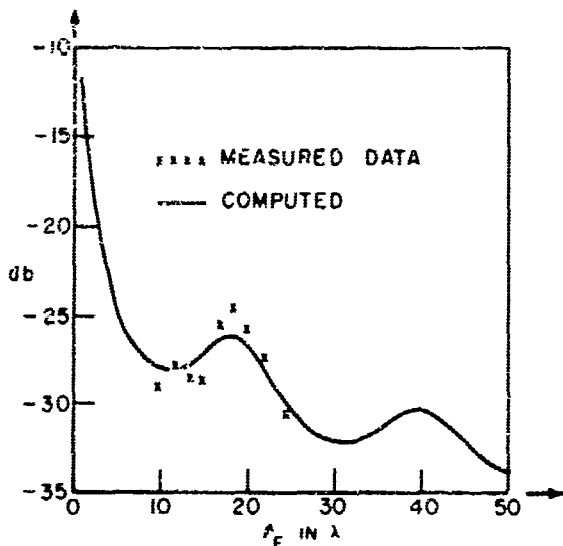


Fig. 9. Back-to-front ratio of  $2\theta_E = 35^\circ$ .

points where minimum back-to-front ratios occur. For a horn antenna with  $\theta_0 = 25^\circ$ , and  $\rho_E = 6.5\lambda, 17\lambda, 27\lambda, 38\lambda$ , and  $48\lambda$ , where minima take place in Fig. 8, the main beam of the pattern is split into two, four, six, eight, and ten lobes, respectively. As for EMC problems, Fig. 8 can be used to evaluate approximately the representative back-radiation intensity  $u(\pi)$  relative to front-radiation intensity  $u(0)$ . If the horn antenna is large enough, it is generally safe to expect that the radiation intensity on the average in the region  $90^\circ < \theta < 180^\circ - \theta_E$  is about 5 db lower than the representative value  $u(\pi)$  as shown in Figs. 8 and 9.

## VII. CONCLUSIONS

The E-plane patterns, including far-sidelobes and backlobes, of horn antennas has been formulated without employing aperture methods and equivalence principles. Considering the various assumptions and the mathematical difficulties inherent in aperture methods it is shown here that diffraction theory is more accurate and practical in analyzing radiation characteristics of typical horn antennas.

The pattern of the proposed reflector model may, in theory, be computed by Eq. (18) as accurately as desired. For reflectors of typical dimensions, the approximated pattern in Eq. (29) has been shown

in Figs. 5, 6, and 7 to be in excellent agreement with the measured patterns of horn antennas for which the reflector model is intended. Comparisons with the first-order patterns indicate that the improvements of Eq. (29) are mainly in the far-sidelobes and backlobes. As a consequence of the approximations made to obtain Eq. (29), the pattern level tends to deviate more and more in the region around  $\theta = 90^\circ - \theta_E$ , when horn dimensions become smaller. Figure 7 shows that the second-order image terms in Eq. (15) can no longer be assumed negligible for small horns. In conclusion, Eq. (29) is generally sufficient to predict patterns of typical horn antennas. If higher accuracy is desired, the higher-order terms neglected in Eq. (29) may be included for computation.

The curves of backlobe levels in Figs. 8 and 9 are approximated by the first-order diffraction terms. More accurate prediction of back-to-front ratios should include all higher-order terms which have significant contribution in the back-lobe region.

#### ACKNOWLEDGEMENTS

Gratitude is expressed to Dr. Leon Peters, Jr., for his suggestions. Thanks are due to Mr. Curtis H. Davis for the measurements and Mr. Marion L. Tripp for the computations.

## APPENDIX A REVIEW OF DIFFRACTION THEORY

The two-dimensional problem of the electromagnetic field in the neighborhood of a conducting wedge illuminated by a uniform plane wave was first solved by Sommerfeld[7]. The solution for a conducting half-plane (zero wedge angle) was formulated in terms of the Fresnel integral. Subsequently, Pauli[8] formulated the solution for wedges of arbitrary angles in an asymptotic series in which the dominant term is the Fresnel integral. The higher-order terms in Pauli's solution become identically zero for zero wedge angle. Therefore, Pauli's solution is used here for the general case.

Figure 10a shows the geometry of the wedge used by Pauli to formulate the solution of field intensity at  $P(r, \psi)$  caused by plane-wave illumination. By reciprocity, if the same wedge of a perfectly conducting surface is illuminated by a uniform cylindrical wave from  $S$  shown in Fig. 10b, the far-field intensity can be written from Pauli's solution as

$$(30) \quad v = v(\rho, \phi^+, n) \pm v(\rho, \phi^-, n),$$

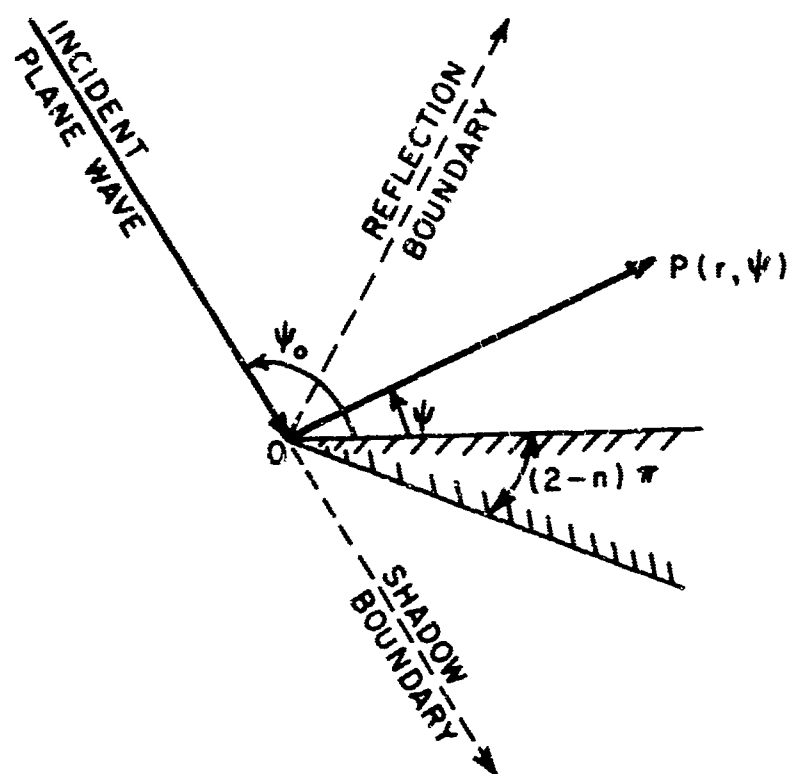
$$= v^+ \pm v^-$$

$$\phi^\pm = \psi \mp \psi_0, \text{ and}$$

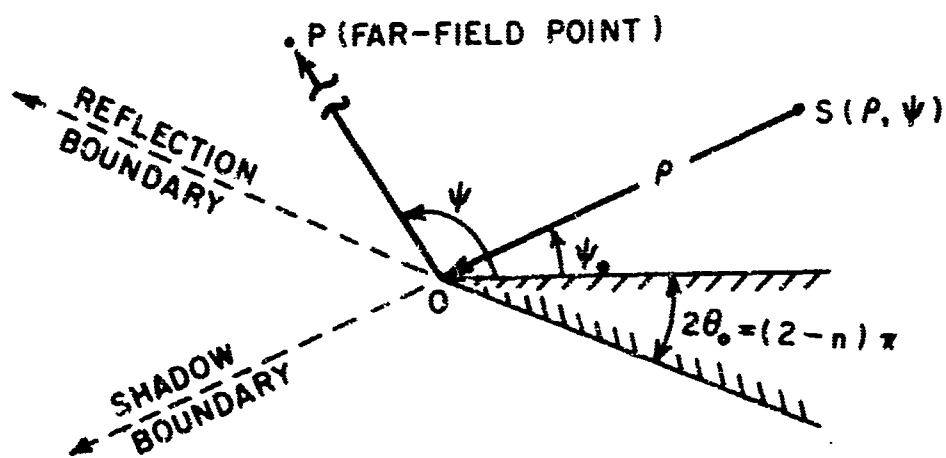
$$n = 2 - \frac{2\epsilon_0}{\pi},$$

where the terms  $v^\pm$  represent the incident and the reflected fields, respectively. The sum  $(v^+ + v^-)$  applies when  $S$  is a magnetic line source, and the difference  $(v^+ - v^-)$  applies if  $S$  is an electric line source. The incident and the reflected fields are composed of geometrical optics terms and diffracted terms, as,

$$v^\pm = (v^*)^\pm + v_B^\pm.$$



(a) Illuminated by a uniform plane wave



(b) Illuminated by uniform cylindrical wave

Fig. 10. Geometry of a wedge.

The geometrical optics terms are given by

$$(31) \quad (v^*)^\pm = v^*(\rho, \phi^\pm, n) \\ = \begin{cases} \text{Exp}[jk\rho \cos(\phi^\pm + 2\pi nN)], & -\pi < \phi^\pm + 2\pi nN \leq \pi, \\ 0 & \text{otherwise} \end{cases}$$

$$N = 0, \pm 1, \pm 2, \dots,$$

where the periodicity of the functions is seen to be  $2\pi n$ . The diffracted terms are given by

$$(32) \quad v_B^\pm = v_B(\rho, \phi^\pm, n) \\ = \frac{\text{Exp}(j\frac{\pi}{4})}{\sqrt{\pi}} \left( \frac{\sin \frac{\pi}{n}}{n} \right) \left[ \frac{2 \left| \cos \frac{\phi^\pm}{2} \right| \text{Exp}(jk\rho \cos \phi^\pm)}{\cos \frac{\pi}{n} - \cos \frac{\phi^\pm}{n}} \int_{jk\rho}^{\infty} e^{-j\tau^2} d\tau \right. \\ \left. + \left( \begin{array}{l} \text{Higher-order terms} \\ \text{negligible for large } kp \end{array} \right) \right]$$

and

$$a = 1 + \cos \phi^\pm.$$

As  $(kp)$  approaches infinity, i.e., as the line source  $S$  recedes to the far-zone, the solutions in Eq. (32) can be written

$$(33) \quad v_B(\rho, \phi^\pm, u) = \frac{\text{Exp}[-j(\frac{\pi}{4} + kp)]}{\sqrt{2\pi kp}} \left[ \frac{\sin \frac{\pi}{n}}{n(\cos \frac{\pi}{n} - \cos \frac{\phi^\pm}{n})} \right].$$

For  $N=0$  in Eq. (31), the geometrical optics terms have discontinuities at the shadow boundary ( $\phi^+ = \pi$ ), and the reflection boundary ( $\phi^- = \pi$ ). At these boundaries, the diffracted terms are given as

$$(34) \quad v_B(p, \phi^{\pm} = \pi, n) = \begin{cases} -\frac{1}{2} \text{Exp.}(-jk\rho) + \dots & \phi^{\pm} \approx \lim(\pi - \epsilon) \\ & \epsilon \rightarrow 0 \\ +\frac{1}{2} \text{Exp.}(-jk\rho) + \dots & \phi^{\pm} \approx \lim(\pi + \epsilon) \\ & \epsilon \rightarrow 0 \end{cases}$$

where the higher-order terms are negligible for large ( $k\rho$ ) are not presented. The solutions are essential in ensuring continuity at the boundaries. Since we intentionally make the geometrical optics terms in Eq. (31) defined at the boundaries,  $\phi^{\pm} = \pm\pi$ , the first equation of Eq. (34) should be used to obtain the field intensities at the boundaries. The total far-field of the wedge illuminated by a uniform cylindrical wave shown in Fig. 10b can now be obtained by using Eqs. (31), (32), and (34) as

$$(35) \quad u(p, \phi, n) = [(v^*)^+ + v_B^+] \pm [(v^*)^- + v_B^-],$$

where the reflection terms disappear if the wedge is illuminated by the source with  $\psi_0 = 0$ . If the source is an electric line element, the value of  $u(p, \phi, n)$  is identically zero for  $\psi_0 = 0$ .

The solutions in Eq. (35) are valid only in evaluating the far-field intensity which is the main concern of present problem. The diffracted near-field intensities of a conducting half-plane, i.e.,  $n = 2$ , have been solved by Nomura[9] and used by Ohba for dipole source illumination. Since this solution is in a general form, it can easily serve to illustrate principles of reciprocity. To generalize the solution further, the diffracted near-fields of a wedge illuminated by a line source have been written by Dybdal[10] in a form as follows:

$$(36) \quad v(r, p, \phi^{\pm}, n) = \frac{\text{Exp}[-jk(r+p-b)]}{\sqrt{r+p}} [v_B(b, \phi^{\pm}, n)]$$

$$b = \frac{rp}{r+p},$$

where the  $v_B$  terms are given in Eq. (32). If the field point is in the far-zone,  $v(r, p, \phi^{\pm}, n)$  is reduced to

$$v(r, \rho, \phi^t, n) = \frac{\text{Exp}[-jkr]}{\sqrt{r}} [v_B(\rho, \phi^t, n)],$$

which, with the common factor  $r^{-\frac{1}{2}} \text{Exp}[-jkr]$  removed, is identical to Eq. (32). If the source point recedes to the far-zone, the solutions in Eq. (36) are reduced to

$$v(r, \rho, \phi^t, n) \approx \frac{\text{Exp}[-jk\rho]}{\sqrt{\rho}} [v_B(r, \phi^t, n)],$$

which, with the common factor  $\rho^{-\frac{1}{2}} \text{Exp}[-jk\rho]$  removed, are identical to the near-field solutions of a wedge illuminated by a uniform plane wave.

APPENDIX B  
FAR-FIELD WAVES FROM THE IMAGES  
OF LINE SOURCES

Consider line sources parallel to perfectly conducting plane walls. The problem in this Appendix is to obtain the far-field intensity of the image waves from the walls. The problem is a two-dimensional one and the line sources can be either magnetic or electric line sources.

First, a directional line source is shown at point  $S$  in Fig. 11. If a semi-infinite conducting wall is placed with an angle  $\theta_0$  with respect to the horizontal reference axis, the image of the line source is formed at point  $l$ . The line source radiates a directional cylindrical wave to the

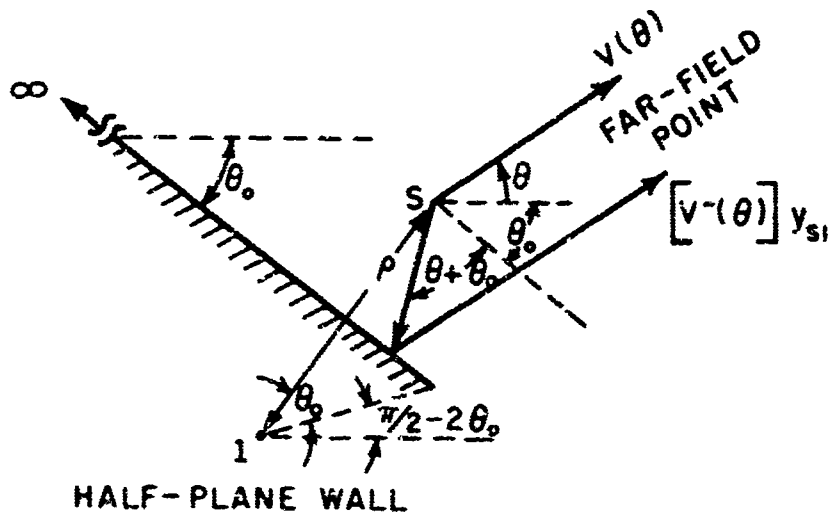


Fig. 11. Geometry of a line source and its image.

far-field and it is designated as  $v(\theta)$ . In the presence of the wall,  $v(\theta)$  is reflected by the wall in the region  $-(\pi + \theta_0) \leq \theta \leq -\pi/2$ . The reflected wave is called the image wave from point  $l$  and can be described by

$$(37) \quad I_l(\theta) = v^-(\theta) = v(-2\theta_0 - \theta), \quad \frac{\pi}{2} - 2\theta_0 \leq \theta \leq -(\pi - \theta_0),$$

where the superscript minus sign implies the reflection of  $v(\theta)$ . The total far-field pattern can then be obtained by superposition of the two waves as

$$(38) \quad u(\theta) = v(\phi) \pm v(-2\theta_0 - \theta) y_{s1}$$

and

$$y_{s1} = \text{Exp}[-jk\rho \sin(\theta + \theta_0)],$$

where  $y_{s1}$  is the local phase-factor of the image referred to point S and  $\rho$  is the distance between the image and the source as shown in Fig. 11. This result is obtained by removing the common factor  $R^{-\frac{1}{2}} \text{Exp}[-jkR]$ , with R referred to S. The plus sign applies for a magnetic line source, while the minus sign should be used for an electric line source.

Next, a corner reflector of  $2\theta_0$  is shown in Fig. 12a. Let there be only one line source  $v(\theta)$  at A. In the region  $-(\pi - \theta_0) < \theta < -\pi/2$ , the rays from A are reflected by the lower wall. Only rays in the ray -1 zone (from image -1) are directly reflected to the far-field. The rays in ray -2 zone are reflected twice while those in ray -3 zone are reflected three times inside the reflector. Consequently, three image waves are formed in three distinct regions. The first image wave can be written similar to Eq. (37) from Fig. 12a as

$$(39) \quad v_1^-(\theta) = v(-2\theta_0 - \theta), \quad \frac{\pi}{2} - 2\theta_0 \leq \theta \leq \frac{\pi}{2} - \theta_0,$$

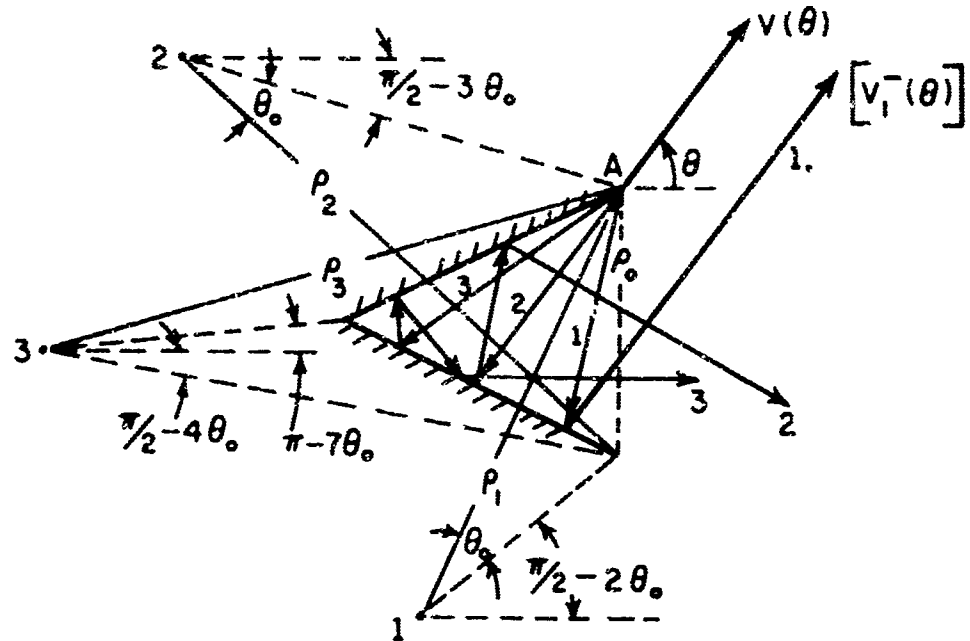
which is obtained by replacing the  $\theta$  of  $v(\theta)$  by  $(-2\theta_0 - \theta)$ . The second image is formed in the upper wall. This image wave can be obtained by replacing the  $\theta$  of  $v_1^-(\theta)$  by  $(+2\theta_0 - \theta)$  as

$$(40) \quad v_2^-(\theta) = v(-4\theta_0 + \theta), \quad -\left(\frac{\pi}{2} - 3\theta_0\right) \geq \theta \geq -\left(\frac{\pi}{2} - 2\theta_0\right).$$

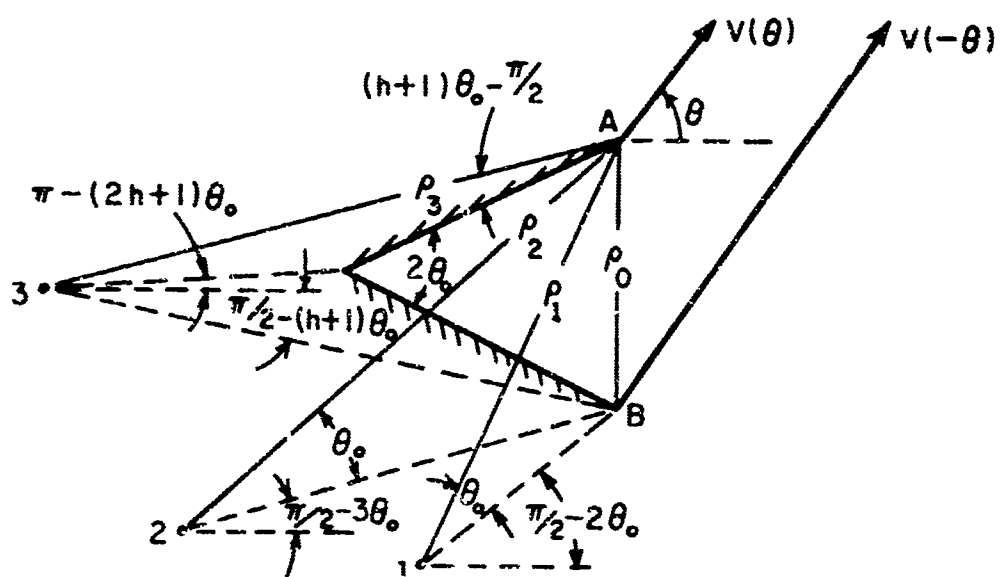
Again replacing the  $\theta$  of the above expression by  $(-2\theta_0 - \theta)$ , the third image wave can be obtained as

$$v_3^-(\theta) = v(-6\theta_0 - \theta), \quad \frac{\pi}{2} - 4\theta_0 \leq \theta \leq \pi - 7\theta_0.$$

This process can be used for any number of images. The number of images is equal to the number of ray zones determined by the highest integer  $h$  such that  $h < \pi/2\theta_0$ . Construction of the images in Fig. 12a can



(a) Images due to a line source at A



(b) Images of lower wall due to two symmetrical line sources

Fig. 12. Geometry of a corner reflector  $\frac{\pi}{3} > 2\theta_0 > \frac{\pi}{4}$ .

be extended to conclude that all the odd-numbered images are formed in the lower wall, while the even-numbered images are in the upper wall. In general, the image waves can be written

$$(41) \quad v_i^-(\theta) = \begin{cases} v(-2i\theta_0 - \theta) & \frac{\pi}{2} - (i+1)\theta_0 \leq \theta \leq \frac{\pi}{2} - i\theta_0 \quad \text{for } i \text{ odd} \\ v(-2i\theta_0 + \theta) & -[\frac{\pi}{2} - (i+1)\theta_0] \geq \theta \geq -[\frac{\pi}{2} - i\theta_0] \quad \text{for } i \text{ even,} \end{cases}$$

$i = 1, 2, 3, \dots, (h-1)$ .

If the ratio of  $\pi$  to  $2\theta_0$  is not exactly an integer, the valid region of the last image should be modified as

$$(42) \quad v_h^-(\theta) = \begin{cases} v(-2h\theta_0 - \theta) & \frac{\pi}{2} - (h+1)\theta_0 \leq \theta \leq \pi - (2h+1)\theta_0 \quad h \text{ odd} \\ v(-2h\theta_0 + \theta) & -[\frac{\pi}{2} - (h+1)\theta_0] \geq \theta \geq -[\pi - (2h+1)\theta_0] \quad h \text{ even.} \end{cases}$$

The value of  $2\theta_0$  in Fig. 12 is larger than  $\pi/4$  but smaller than  $\pi/2$ . Therefore  $h$  is equal to 3 and the last image is defined by Eq. (42) for  $h$  odd.

Figure 12b shows two symmetrical line sources at A and B from which far-field waves  $v(\theta)$  and  $v(-\theta)$ , respectively, are radiated. The images of the source at A are identical to those in Fig. 12. Because of the symmetrical properties of the assumed line sources and the geometry of the reflector, the images resulting from the source at B are symmetrical to those of A. Consequently, equal numbers of symmetrical images are formed in both walls of the reflector. Making use of this symmetry, the image waves excited by  $v(-\theta)$  from B can be obtained similar to Eq. (41) as

$$(43) \quad v_i^-(\theta) = \begin{cases} v(-2i\theta_0 + \theta) & -[\frac{\pi}{2} - (i+1)\theta_0] \geq \theta \geq -[\frac{\pi}{2} - i\theta_0] \quad i \text{ odd} \\ v(-2i\theta_0 - \theta) & \frac{\pi}{2} - (i+1)\theta_0 \leq \theta \leq \frac{\pi}{2} - i\theta_0 \quad i \text{ even,} \end{cases}$$

$i = 1, 2, 3, \dots, (h-1)$ .

In case the ratio  $\pi$  to  $2\theta_0$  is not an integer, the last image wave has its defined region as in Eq. (42) by interchanging  $h$  odd and  $h$  even.

Comparison of Eqs. (41) to (43) indicates that all image waves from the lower wall are combinations of  $v_i^-(\theta)$  with  $i$  odd and  $v_i^-(-\theta)$  with  $i$  even. The other set of combinations gives the image waves from the upper wall. To summarize, the image waves from both walls of the reflector are designated by  $(I_L)_i$  and  $(I_U)_i$  as follows:

$$(44) \quad (I_L)_i = v^-(\theta) = v(-2i\theta_0 - \theta), \quad \frac{\pi}{2} - (i+1)\theta_0 \leq \theta \leq \frac{\pi}{2} - i\theta_0, \quad \text{lower wall};$$

$$(I_U)_i = v^-(-\theta) = v(-2i\theta_0 + \theta), \quad -[\frac{\pi}{2} - (i+1)\theta_0] \geq \theta \geq -[\frac{\pi}{2} - i\theta_0], \quad \text{upper wall};$$

$$i = 1, 2, 3, \dots, h.$$

For the ratio of  $\pi$  to  $2\theta_0$  not an integer, modifications for  $i = h$  are

$$(45) \quad (I_L)_h = v(-2h\theta_0 - \theta), \quad \frac{\pi}{2} - (h+1)\theta_0 \leq \theta \leq \pi - (2h+1)\theta_0;$$

and

$$(I_U)_h = v(-2h\theta_0 + \theta), \quad -[\frac{\pi}{2} - (h+1)\theta_0] \geq \theta \geq -[\pi - (2h+1)\theta_0].$$

In Fig. 12b, three images in the lower wall are shown. Their far-field intensities can be obtained by setting  $h = 3$  in Eqs. (44) and (45).

Because of symmetry, only the upper-half region  $0 \leq \theta \leq \pi$  needs to be considered for the radiation pattern of the reflector antenna. In this region, the contributions are from the sources at A and B and the images in the lower wall. Contributions from the last image in the upper wall are possible, if the ratio of  $\pi$  to  $2\theta_0$  is not an integer. Superposition of all these contributions gives the total far-field  $u(\theta)$  as

$$(46) \quad u(\theta) = v(\theta) + [v(-\theta)]y_{AB} + \sum_{i=1}^h (\pm 1)^i [v(-2i\theta_0 - \theta)]y_{Ai} \\ + (\pm 1)^h [v(-2h\theta_0 + \theta)]y_{AB} y_{Bh},$$

where  $(+1)^i$  preceding the image terms are used for magnetic line sources and  $(-1)^i$  are used for electric line sources. The phase factors are introduced by taking A as phase-reference:

$$(47) \quad \begin{aligned} y_{AB} &= \text{Exp} [-jk\rho_0 \sin \theta], \\ y_{Ai} &= \text{Exp} [-jk\rho_i \sin (i\theta_0 + \theta)], \\ y_{Bh} &= \text{Exp} [-jk\rho_h \sin (h\theta_0 - \theta)], \\ \rho_0 &= AB, \text{ and} \\ \rho_i &= \rho_{i-1} \cos \theta_0 + \rho_0 \cos (i\theta_0). \end{aligned}$$

The above expressions can be obtained by considering the geometry of Fig. 12. It is noted that each term in Eqs. (45) and (47) is set zero outside its defined region.

APPENDIX C  
COUPLING COEFFICIENTS OF THE FOUR WEDGES  
OF THE ANTENNA MODEL

The primary source at S in Fig. 1 illuminates wedges A and B. The resulting diffractions are denoted as first-order. When the first-order-induced line source at A illuminates B, W, and S, the diffractions are designated as second-order. Likewise, A, W, and S are illuminated by the first-order-induced source at B. Therefore, the lowest order of diffractions for W and S in our present problem is second-order.

Physical significance of the coupling coefficients in Eq. (17) can be more clearly stated by taking  $C_{AB}^{(m-1)}$  as example. Wedge B is illuminated by the  $(m-2)^{th}$ -induced sources at A, W, S, and  $(h-1)$  images. There are then  $(h+2)$  terms of  $(m-1)^{th}$ -order diffraction waves induced at wedge B. Combination of these  $(h+2)$  terms forms a directional cylindrical wave radiated from B. In the direction of wedge A,  $\theta = +\pi/2$ , the illumination intensity is therefore a combination of  $(h+2)$  terms in this direction. Writing out these terms yields

$$C_{AB}^{(m-1)} = C_{BA}^{(m-2)} C_{ABA} + C_{BW}^{(m-2)} C_{ABW} + C_{BS}^{(m-2)} C_{ABS} \\ + \sum_{i=1}^{h-1} C_{Bi} C_{ABI},$$

where the double subscripts denote  $(m-2)^{th}$ -order illuminations from various sources to B. The triple subscript terms denote coupling coefficients from various sources through B to A. Similarly, for other wedges and the images, symmetry property can be used to obtain

$$(48) \quad C_{BA}^{(m-1)} = C_{AB}^{(m-2)} C_{BAB} + C_{AW}^{(m-2)} C_{BAW} + C_{AS}^{(m-2)} C_{BAS} \\ + \sum_{i=1}^{h-1} C_{Ai}^{(m-2)} C_{BAi} = C_{AB}^{(m-1)}.$$

$$(48) \quad (cont) \quad C_{Ai}^{(m-1)} = C_{AB}^{(m-2)} C_{AiA} + C_{AW}^{(m-2)} C_{AiW} + C_{AS}^{(m-2)} C_{AiS}$$

$$+ \sum_{k=1}^{h-1} C_{Ak}^{(m-2)} C_{Aik} = B_{Bi}^{(m-1)},$$

$$C_{AW}^{(m-1)} = C_{WA}^{(m-2)} C_{AWA} + C_{WB}^{(m-2)} C_{AWB} = C_{BW}^{(m-2)},$$

$$C_{AS}^{(m-1)} = C_{SA}^{(m-2)} C_{ASA} + C_{SB}^{(m-2)} C_{ASB} = C_{BS}^{(m-2)},$$

$$C_{WA}^{(m-1)} = C_{AB}^{(m-2)} C_{WAB} + C_{AW}^{(m-2)} C_{WAW} + C_{AS}^{(m-2)} C_{WAS}$$

$$+ \sum_{i=1}^{h-1} C_{Ai}^{(m-2)} C_{WAi} = C_{WB}^{(m-1)},$$

$$C_{SA}^{(m-1)} = C_{AB}^{(m-2)} C_{SAB} + C_{AW}^{(m-2)} C_{SAW} + C_{AS}^{(m-2)} C_{SAS}$$

$$+ \sum_{i=1}^{h-1} C_{Ai}^{(m-2)} C_{SAi} = C_{SB}^{(m-1)},$$

$$m = 3, 4, 5, \dots, \infty.$$

Equation (48) applies only for  $m \geq 3$ . For  $m = 1$ , the coupling coefficients are of zero-order and are not defined for our problem except for direct illumination from the primary source at S. For  $m = 2$ , the coupling coefficients are of first-order and are given in Formulation of Solution as

$$(49) \quad C_{BA}^{(1)} = C_{AB}^{(1)} = v_B \left( \rho_E, \frac{\pi}{2} - \theta_0 \right),$$

$$C_{WA}^{(1)} = C_{WB}^{(1)} = v_B (\rho_E, 2\pi),$$

$$C_{SA}^{(1)} = C_{SB}^{(1)} = v_B (\rho_E, 0),$$

and

$$C_{Ai}^{(1)} = C_{Bi}^{(1)} = v_B \left( \rho_E, \frac{\pi}{2} - (i+1)\theta_0 \right), \quad i = 1, 2, \dots, (h-1).$$

The  $C_{AW}^{(m-1)}$ ,  $C_{BW}^{(m-1)}$ , and  $C_{AS}^{(m-1)}$ ,  $C_{BS}^{(m-1)}$  are equal to zero, for  $m = 2$ , because there are no first-order induced sources at W and S. For  $m = 3$ , Eq. (48) can be written as

$$(50) \quad C_{BA}^{(2)} = C_{AB}^{(1)} C_{BAB} + \sum_{i=1}^{h-1} C_{Ai}^{(1)} C_{BAi} = C_{AB}^{(2)},$$

$$C_{Ai}^{(2)} = C_{AB}^{(1)} C_{AiB} + \sum_{k=1}^{h-1} C_{Aik}^{(1)} C_{Aik} = C_{Bi}^{(2)},$$

$$C_{AW}^{(2)} = C_{WA}^{(1)} C_{AWA} + C_{WB}^{(1)} C_{AWB} = C_{BW}^{(2)},$$

$$C_{AS}^{(2)} = C_{SA}^{(1)} C_{ASA} + C_{SB}^{(1)} C_{ASB} = C_{BS}^{(2)},$$

$$C_{WA}^{(2)} = C_{AB}^{(1)} C_{WAB} + \sum_{i=1}^{h-1} C_{Ai}^{(1)} C_{WAi} = C_{WB}^{(2)},$$

and

$$C_{SA}^{(2)} = C_{AB}^{(1)} C_{SAB} + \sum_{i=1}^{h-1} C_{Ai}^{(1)} C_{SAi} = C_{SB}^{(2)},$$

where the triple-subscript coupling coefficients can be obtained from the variable terms in Eq. (17) as

$$(51) \quad C_{BAE}, C_{WAB}, C_{SAB} = v_B(b, \frac{\pi}{2} + \theta) + v_B(b, \frac{3\pi}{2} - 2\theta_0 + \theta),$$

$$\text{at } \theta = -\frac{\pi}{2}, \pi + \theta_0, -(\pi - \theta_0);$$

$$C_{BAW}, C_{WAW}, C_{SAW} = v_B(p_E, \pi + \theta_0 - \theta),$$

$$\text{at } \theta = -\frac{\pi}{2}, \pi + \theta_0, -(\pi - \theta_0);$$

$$C_{BAS}, C_{WAS}, C_{SAS} = v_B(p_E, \pi - \theta_0 + \theta),$$

$$\text{at } \theta = -\frac{\pi}{2}, \pi + \theta_0, -(\pi - \theta_0);$$

$$C_{BAi}, C_{WAi}, C_{SAi} = v_B(p_i, \frac{\pi}{2} + i\theta_0 + \theta) + v_B(p_i, \frac{3\pi}{2} - (i+2)\theta_0 + \theta),$$

$$\text{at } \theta = -\frac{\pi}{2}, \pi + \theta_0, -(\pi - \theta_0);$$

$$C_{AiB} = v_B(b, \frac{\pi}{2} - 2i\theta_0 - \theta) + v_B(b, \frac{3\pi}{2} - 2(i+1)\theta_0 - \theta),$$

$$\text{at } \theta = \left(\frac{\pi}{2} - i\theta_0\right);$$

$$C_{AiW} = v_B(p_E, \pi + (2i+1)\theta_0 + \theta), \quad \text{at } \theta = \frac{\pi}{2} - i\theta_0;$$

$$C_{AiS} = v_B(p_E, \pi - (2i+1)\theta_0 - \theta), \quad \text{at } \theta = \frac{\pi}{2} - i\theta_0;$$

$$C_{Aik} = v_B(p_k, \frac{\pi}{2} - i\theta_0 - \theta) + v_B(p_k, \frac{3\pi}{2} - (3i+2)\theta_0 - \theta),$$

$$\text{at } \theta = \frac{\pi}{2} - i\theta_0;$$

$$C_{AWA} = v_B(p_E, \theta - \theta_0, v_W) \text{ at } \theta = \theta_0;$$

$$C_{AWB} = v_B(p_E, 2\pi - \theta - \theta_0, n_W) \text{ at } \theta = \theta_0;$$

(51)  
(cont)  $C_{ASA} = v_B(\rho_E, \theta_0 + \theta), \text{ at } \theta = \theta_0;$

and

$$C_{ASB} = v_B(\rho_E, \theta_0 - \theta), \text{ at } \theta = \theta_0.$$

Equations (49), (50), and (51) can then be used to solve any order of coupling coefficients from Eq. (48).

## APPENDIX D THE SCATRAN SOURCE PROGRAMS FOR NUMERICAL COMPUTATION BY IEM 7094

The source programs for Eq. (29) and the associated subroutine  $v_B$  are presented here for reference. The input data required are the horn length  $\rho_E$  in terms of wavelength and the angle  $\theta_E$  in degrees.

It is noted that the notations  $Q$ ,  $R$ ,  $r_E$ , and  $\alpha_E$  in the programs correspond to  $A$ ,  $B$ ,  $\rho_E$ , and  $\theta_E$ , respectively, in Fig. 1.

```

        INTEGERS (H)-
        FLOATING (NS+NW)-
        COMPLEX (CQRQ,CQRI,SCUR1,CWQ2,CWQ1,SCWQ1)-
        COMPLEX (YR+XRSB+T3P)-
        COMPLEX (CWQ,CQR,CQ,XQS+XQR,XQ+XRS+XQ,XR+XRSP)-
        COMPLEX (XRQP,XRP+XWQ,XWR,XQSB+YQS+YQR,YQ+UR+UT)-
        COMPLEX (COMZ+T1+T2+T3)-
        COMPLEX (CEXPL)-
        DIMENSION (R(200),CQ(200),XQ(200),XR(200),XRP(200))-
        DIMENSION (XQSB(200),YQ(200))-
        LITERALS (PI+3+14159265+RAD+0.01745329,PI2+6+2831853)-
        DIMENSION (YR(200),XRSB(200))-
        LITERALS (COMZ+0+I+0+PIOH+1+5707963)-
C ***** H01
        INPUT -
        READ INPUT +8+(NCS)-
        DO THROUGH (H23),IN=0+1+IN+L+NCS-
        READ INPUT +HFO1+(RE+ALPHE)-
C *****
        CALCULATION OF CONSTANTS -
        ALR=RAD*ALPHE-
        H=PI/12+ALR)-
        PROVIDED (H+E+PI/(2+ALR))+H=H-1-
        NS=(2+ALR)/PI-
        NW=(2-NS)-
        R=2+RE*SIN+(ALR)-
        B=R-
        DO THROUGH (H02),I=1+1+I+LE+H-
        R(I)=R(I-1)+COS+(ALR)+R*COS+(I*ALR)-
        TRANSFER (H02) PROVIDED (I+GE+H)-
        CALL SUBROUTINE (RVB+UVB)=VB+(PI2+RE+PIOH-(I+1)*ALR+2+)
        CQ(I)=RVB+I+UVB-
        CONTINUE -
        CALL SUBROUTINE (RVB+UVB)=VB+(PI2+8+PI-2+ALR+2+)
        CQRQ=RVB+I+UVB-
        CALL SUBROUTINE (RVB+UVB)=VB+(PI2+8+0+2+)
        CQRQ=CQRQ+(RVB+I+UVB)-
        CALL SUBROUTINE (RVB+UVB)=VB+(PI2+RE+PIOH-ALR+2+)
        CQRI=RVB+I+UVB-
        SCQRI=COMZ-
        DO THROUGH (H02A),I=H-1+1+I+GE+1-
        CALL SUBROUTINE (RVB1+UVB1)=VB+(PI2+R(I)+I*ALR+2+)
        CALL SUBROUTINE (RVB+UVB)=VB+(PI2+R(I)+PI-(I+2)*ALR+2+)
        RVB1=RVB1+RVB-
        UVB1=UVB1+UVB-
        CALL SUBROUTINE (RVB+UVB)=VB+(PI2+RE+PIOH-(I+1)*ALR+2+)
        SCQRI=SCQRI+(RVB1+I+UVB1)*(RVB+I+UVB)-
        CQR=(CQRI+SCQRI)/((1+I+0+)-CQRQ)-
        CALL SUBROUTINE (RVB+UVB)=VB+(PI2+8+3+*PIOH+ALR+2+)
        CWQ2=RVB+I+UVB-
        CALL SUBROUTINE (RVB+UVB)=VB+(PI2+8+5+*PIOH-ALR+2+)
        CWQ2=(CWQ2+(RVB+I+UVB))*CQR-
        CALL SUBROUTINE (RVB+UVB)=VB+(PI2+RE+PI2+2+)
        CWQ1=RVB+I+UVB-
        SCWQ1=COMZ-
        DO THROUGH (H02B),I=H-1+1+I+GE+1-
        CALL SUBROUTINE (RVB1+UVB1)=VB+(PI2+R(I)+3+*PIOH+(I+1)*ALR
        +2+)
        CALL SUBROUTINE (RVB+UVB)=VB+(PI2+R(I)+5+*PIOH-(I+1)*ALR+2
        +)
        RVB1=RVB1+RVB-
        UVB1=UVB1+UVB-
        CALL SUBROUTINE (RVB+UVB)=VB+(PI2+RE+PIOH-(I+1)*ALR+2+)
        SCWQ1=SCWQ1+(RVB+I+UVB)*(RVB+I+UVB)-
        CWQ=CWQ1+CWQ2+SCWQ1-
C *****
        CALCULATION OF VARIABLES -

```

```

        DO THROUGH (H22),K=0,1,K+LE+180-
        THETA=K*RAD-
        CALL SUBROUTINE (RVB+UVB)=VB.(PI2*RE*PI-ALR+THETA+2.0)-
        XQS=RVB+.I*UVB-
        CALL SUBROUTINE (RVB+UVB)=VB.(PI2*R*PIOH+THETA+2.0)-
        XQR=RVB+.I*UVB-
        CALL SUBROUTINE (RVB+UVB)=VB.(PI2*R+3.*PIOH-2.*ALR+THETA+2
        .0)-
        XQR=XQR+(RVB+.I*UVB)-
        YQS=CEXPL.(0.+.I.-PI2*RE*COS.(THETA-ALR))-.
        YQR=CEXPL.(0.+.I.-PI2*R*SIN.(THETA))-.
        DO THROUGH (H03),I=H-1,-1+I,GE+1-
        CALL SUBROUTINE (RVB+UVB)=VB.(PI2*R(I)+PIOH+I*ALR+THETA+2
        .0)-
        XQ(I)=RVB+.I*UVB-
        CALL SUBROUTINE (RVB+UVB)=VB.(PI2*R(I)+3.*PIOH-(I+2)*ALR+T
        HETA+2.0)-
        XQ(I)=XQ(I)+(RVB+.I*UVB)-
        S=1.-
        PROVIDED (THETA+G+ALR)+S=0.-
        TRANSFER (H05) PROVIDED (THETA+G+PIOH)-
        CALL SUBROUTINE (RVB+UVB)=VB.(PI2*RE*PI-ALR-THETA+2.0)-
        XRS=RVB+.I*UVB-
        CALL SUBROUTINE (RVB+UVB)=VB.(PI2*R+PIOH-THETA+2.0)-
        XRQ=RVB+.I*UVB-
        CALL SUBROUTINE (RVB+UVB)=VB.(PI2*R+3.*PIOH-2.*ALR-THETA+2
        .0)-
        XRG=XRQ+(RVB+.I*UVB)-
        DO THROUGH (H04),I=H-1,-1+I,GE+1-
        CALL SUBROUTINE (RVB+UVB)=VB.(PI2*R(I)+PIOH+I*ALR-THETA+2
        .0)-
        XR(I)=RVB+.I*UVB-
        CALL SUBROUTINE (RVB+UVB)=VB.(PI2*R(I)+3.*PIOH-(I+2)*ALR-T
        HETA+2.0)-
        XR(I)=XR(I)+(RVB+.I*UVB)-
        TRANSFER (H07)-
        H05
        XRS=COMZ-
        XRG=COMZ-
        DO THROUGH (H06),I=H-1,-1+I,GE+1-
        XR(I)=COMZ-
        H07
        TRANSFER (H08) PROVIDED (THETA+L+ALR)-
        CALL SUBROUTINE (RVB+UVB)=VB.(PI2*RE*THETA-ALR+NW)-
        XWQ=RVB+.I*UVB-
        CALL SUBROUTINE (RVB+UVB)=VB.(PI2*RE*PI2-THETA-ALR+NW)-
        XWR=RVB+.I*UVB-
        TRANSFER (H09)-
        H08
        XWQ=COMZ-
        XWR=COMZ-
        TRANSFER (H11) PROVIDED (K+L+180.-ALPHE)-
        CALL SUBROUTINE (RVB+UVB)=VB.(PI2*RE+3.*PI-ALR-THETA+2.0)-
        XRSP=RVB+.I*UVB-
        CALL SUBROUTINE (RVB+UVB)=VB.(PI2*R+5.*PIOH-THETA+2.0)-
        XROP=RVB+.I*UVB-
        CALL SUBROUTINE (RVB+UVB)=VB.(PI2*R+7.*PIOH-2.*ALR-THETA+2
        .0)-
        XROP=XROP+(RVB+.I*UVB)-
        DO THROUGH (H10),I=H-1,-1+I,GE+1-
        CALL SUBROUTINE (RVB+UVB)=VB.(PI2*R(I)+5.*PIOH+I*ALR-THETA
        +2.0)-
        XRP(I)=RVB+.I*UVB-
        CALL SUBROUTINE (RVB+UVB)=VB.(PI2*R(I)+7.*PIOH-(I+2)*ALR-T
        HETA+2.0)-
        XRP(I)=XRP(I)+(RVB+.I*UVB)-
        TRANSFER (H13)-
        H10

```

```

H11      XRSP=COMZ-
         XROP=COMZ-
         DO THROUGH (H12), I=M-1,-1,1,GE+1-
H12      XRP(I)=COMZ-
         DO THROUGH (H15), I=M-1,-1,1,GE+1-
         TRANSFER (H14) PROVIDED (K+L+90+-(I+1)*ALPHE+OR+K+G+90+-
         1*ALPHE)-

         YQ(I)=CEXPL.(0.++I.+(-PI2*R(I))*SIN.((I+1)*ALR+THETA))-

         CALL SUBROUTINE (RVB+UVB)=VB.(PI2+RE+PI-(2*I+1)*ALR-THETA-
         +2+1)-

         XQSB(I)=RVB++I+UVB-
         TRANSFER (H15)-

H14      YQ(I)=COMZ-
         XQSB(I)=COMZ-
         CONTINUE -
         TRANSFER (H16) PROVIDED (K+L.(2*M+1)*ALPHE-180.+OR+K+G.(M+-
         1)*ALPHE-90+)-

         YR(M)=CEXPL.(0.++I.+(-PI2*R(M))*SIN.((M+1)*ALR+THETA))-

         CALL SUBROUTINE (RVB+UVB)=VB.(PI2+RE+PI-(2*M+1)*ALR+THETA-
         +2+1)-

         XRSB(M)=RVB++I+UVB-
         TRANSFER (H19)-

H16      XRSB(M)=COMZ-
         YR(M)=COMZ-
         CONTINUE -
         TRANSFER (H19A) PROVIDED (K+L+90+-(M+1)*ALPHE+OR+K+G+180+-
         (2*M+1)*ALPHE)-

         CALL SUBROUTINE (RVB+UVB)=VB.(PI2+RE+PI-(2*M+1)*ALR-THETA-
         +2+1)-

         XQSB(M)=RVB++I+UVB-
         YQ(M)=CEXPL.(0.++I.+(-PI2*R(M))*SIN.((M+1)*ALR-THETA))-

         TRANSFER (H19B)-

H19A     XQSB(M)=COMZ-
         YQ(M)=COMZ-
         CONTINUE -
         CALCULATION OF OUTPUT VALUES -
         UR=S*YQ5+XQ5+(XRS+XRSP)*YOR-
         T3P=COMZ-
         T1=COMZ-
         T2=COMZ-
         T3=COMZ-
         DO THROUGH (H20), I=M-1,-1,1,GE+1-
         T1=T1+CQ(I)*XQ(I)-

H20      T2=T2+CQ(I)*(XR(I)+XRP(I))-

         DO THROUGH (H21), I=M-1,-1,1,GE+1-
         T3P=T3P+XQSB(I)*YQ(I)-

H21      T3=T3+XRSB(I)*YR(I)-

         UT=UR+CW0*(XW0+XUR/+YQ5+COR*XOR+T1+(COR*(XRD+XROP)+T2)*YOR+-
         T3+T3P-
         PROVIDED (THETA,NE.0.): TRANSFER (H21A)-
         UR2=CFABS.(UR)-
         UTZ=CFABS.(UT)-
         PRINT-OUT OF VARIABLES -
         IALPHE=10.*ALPHE-
         IRE=10.*RE-
         PUNCH CARDS +HF06.(IALPHE,IRE)-
         CONTINUE -
         FUT=20.*FLOG1.(+ABS.UT/UTZ)-
         FUR=20.*FLOG1.(+ABS.UR/UR2)-
         IFUT(K)=(FUT+90.+)*20.-
         IFUR(K)=(FUR+90.+)*20.-
         KK(K)=6.666667*K-
         DIMENSION (IFUT(181),IFUR(181),KK(181))-
         CONTINUE -

```

H23                    PUNCH CARDS +HF07\*((KK(1)+INPUT(1)+I\*0+1,I+LE,180))-  
F HF01            (2F10.5) -  
F HF05            (2(2X+13)) -  
F HF07            (18I4)-  
                  CALL SUBROUTINE ()=ENDJOB()-  
                  END PROGRAM (H01)-

```

*** SCATRAN                                     RUVB0001
    SUBROUTINE (RVB,UVB)=VB, (FK,ARG,ANGLE,FN) -
    PROVIDED(.ABS(.ABS(ANGLE-3.14159265)*LE,.0001), TRANSFER TO
    (ALTER) -
    CONST = 3.14159265/FN -
    COSANG = COS.(ANGLE) -
    X = FK*ARG*1.+COSANG) -
    CALL FUNCTION (C)=RFRESN.(X) -
    CALL FUNCTION (S)=UFRESN.(X) -
    RCOEFF = COS.(FK*ARG*COSANG) -
    UCOEFF = SIN.(FK*ARG*COSANG) -
    RREST = .5-C/2.-S/2. -
    UREST = S/2.-C/2. -
    COEF=(1./FN)*SIN.(CONST) *2.*.ABS(.1. COS.(ANGLE/2.))/ (COS.(CO
    NST)-COS.(ANGLE/FN)) -
    RVB=COEF*(RCOEFF*RREST-UCOEFF*UREST) -
    UVB=COEF*(RCOEFF*UREST+UCOEFF*RREST) -
    NORMAL EXIT -
    ALTER
    RVB=-.5*COS.(FK*ARG)-
    UVB=+.5*SIN.(FK*ARG)-
    NORMAL EXIT -
    END SUBPROGRAM -
    END PROGRAM -
*** STATEMENT LISTING
*** SCATRAN                                     FRESO001
    FUNCTION (C) = RFRESN.(X) -
    PROVIDED (X.G.10.)* TRANSFER TO (ASYMP) -
    H = SQRT.(2.*X*3.1415927) -
    C = H -
    PROVIDED (.ABS.(H).LE..00001), TRANSFER TO (DONE) -
    DO THROUGH (LOOP), L=1+1, PROVIDED (.ABS.(H).G..00001) -
    H=H*((3.-4.*L)*X*X)/((4.*L+1.)*(2.*L)*(2.*L-1.)) -
    C = C + H -
    LOOP
    CONTINUE -
    TRANSFER TO (DONE) -
    ASYMP
    S1 = 1. -
    AS1 = S1 -
    STEMP1 = .ABS.(S1) -
    DO THROUGH (LOOP1), L=2+2, PROVIDED (.ABS.(S1).G..0001).AND.ST
    EMP1/.ABS.(S1).GE.1. -
    STEMP1 = .ABS.(S1) -
    S1 = S1*((-1.)*(2.*L-1.)*(2.*L-3.))/14.*X*X) -
    AS1 = AS1 + S1 -
    LOOP1
    CONTINUE -
    S2 = .5/X -
    AS2 = S2 -
    STEMP2 = .ABS.(S2) -
    DO THROUGH (LOOP2), L=3 . PROVIDED (.ABS.(S2).G..0001).AND.ST
    EMP2/.ABS.(S2).GE.1. -
    STEMP2 = .ABS.(S2) -
    S2 = S2*((-1.)*(2.*L-3.)*(2.*L-1.))/ (4.*X*X) -
    AS2 = AS2 + S2 -
    LOOP2
    CONTINUE -
    C = .5 + (SIN.(X)/SQRT.(6.2831854*X))*AS1 + (COS.(X)/SQRT.(6
    *2831854*X))*AS2 -
    DONE
    NORMAL EXIT -
    END SUBPROGRAM -
    END PROGRAM -
*** STATEMENT LISTING
*** SCATRAN                                     UFRE0001
    FUNCTION (S) = UFRESN.(X) -
    PROVIDED (X.G.10.)* TRANSFER TO (ASYMP) -

```

```

H = SQRT.(2.*X/3+1415927)*X/3+ -
S = H -
DO THROUGH (LOOP), L=1+1+PROVIDED (.ABS.(H).GE..00001) -
H = H*((1.-4.*L)*X*X)/((4.*L+3.)*(2.*L+1.)*(2.*L)) -
S = S + H -
LOOP CONTINUE -
TRANSFER TO (DONE) -
ASYMP S1 = 1. -
AS1 = S1 -
STEMP1 = .ABS.(S1) -
DO THROUGH (LOOP1), L=2+2+PROVIDED (.ABS.(S1).GE..0001+AND+ST
EMP1/.ABS.(S1).GE.1.) -
STEMP1 = .ABS.(S1) -
S1 = S1*((-1.*(2.*L-1.)*(2.*L-3.))/(4.*X*X)) -
AS1 = AS1 + S1 -
LOOP1 CONTINUE -
S2 = .5/X -
AS2 = S2 -
STEMP2 = .ABS.(S2) -
DO THROUGH (LOOP2), L=3+2+PROVIDED (.ABS.(S2).GE..0001+AND+ST
EMP2/.ABS.(S2).GE.1.) -
STEMP2 = .ABS.(S2) -
S2 = S2*((-1.*(2.*L-3.)*(2.*L-1.))/(4.*X*X)) -
AS2 = AS2 + S2 -
LOOP2 CONTINUE -
S = .5 - (COS.(X)/SQRT.(6.2831854*X))*AS1 - (SIN.(X)/SQRT.(6
+2831854*X))*AS2 -
NORMAL EXIT -
END SUBPROGRAM -
END PROGRAM -

```

## REFERENCES

1. Rhodes, D.R., "An Experimental Investigation of the Radiation Patterns of Electromagnetic Horn Antennas," Proc. IRE, 36, 1101-1105 (September, 1948).
2. Kraus, J.D., Antennas, McGraw-Hill Book Company, Inc., New York, N.Y., (1950), 375-380.
3. Ye Kinber, B., "Diffraction at the Open End of a Sectoral Horn," Radio Engn. and Electronic Physics, 7-10, (October, 1962), 1620-1632.
4. Ohba, Y., "On the Radiation Pattern of a Corner Reflector Finite in Width," IEEE Trans. on Antennas and Propagation, AP-11, 2, (March 1963), 127-132.
5. Russo, P.M., Rudduck, R.C., and Peters, L., Jr., "A Method for Computing E-Plane Pattern of Horn Antennas." To be published in IEEE Trans. on Antennas and Propagation in March, 1965.

Russo, P.M., "Complete Radiation Pattern of the Horn Antenna (Computed by Diffraction Theory)," Report 1767-1, 15 May 1964, Antenna Laboratory, The Ohio State University Research Foundation; prepared under Contract Number AF 30(602)-3269, Air Force Systems Command, Research and Technology Division, Rome Air Development Center, Griffiss Air Force Base, New York.

6. Jasik, H., Antenna Engineering Handbook, McGraw-Hill Book Company, Inc., New York, N.Y. (1961) 10-8.
7. Sommerfeld, A., Optics, Academic Press, Inc., New York, N.Y., (1954), 245-265.
8. Pauli, W., "On Asymptotic Series for Functions in the Theory of Diffraction of Light," Physical Review, 54, (December, 1938), 924-931.
9. Nomura, Y., "On the Diffraction of Electromagnetic Waves by a Perfectly Reflecting Wedge," Res. Inst., Tohoku Univ., Japan; Scientific Repts., B-1 and 2, No. 1, (1951), 1-24.

10. Dybdal, R. B., "Mutual Coupling Between TEM and TE<sub>01</sub> Parallel-Plate Waveguide Aperture," Report 1693-5, August, 1964, 6, Antenna Laboratory, The Ohio State University Research Foundation; prepared under Contract Number N 62269-2184, U. S. Naval Air Development Center, Johnsville, Pennsylvania.